UNIVERSITY OF CALIFORNIA

Los Angeles

Novel strategies for the development of protein delivery platforms

A dissertation submitted in partial satisfaction

of the requirements for the degree Doctor of Philosophy

in Chemical Engineering

by

Jie Ren

2020

ABSTRACT OF THE DISSERTATION

Novel strategies for the development of protein delivery platforms

By

Jie Ren

Doctor of Philosophy in Chemical Engineering

University of California, Los Angeles, 2020

Professor Yunfeng Lu, Chair

Protein are the most dynamic and diverse macromolecules in living organisms, taking part in almost every biological reaction. While burst progresses have been made in revealing new pathways mediated by proteins and understanding of protein functions, their clinical applications are still limited due to the biological barriers that in vivo protein delivery encounters. Although strategies based on nanoparticles have been introduced to address this problem, failure in overcoming all the barriers simultaneously could lead to the compromised delivery efficacy. Therefore, development of delivery platforms that can effectively overcome those biological barriers comprehensively would help realize their potential into practical applications.

In this dissertation, novel strategies have been developed for protein delivery based on coacervate nanoreactors or sheddable PMPC conjugated nanocomplexes depending on the target site of protein therapeutics. This dissertation research consists with two topics outlined below:

1. Realize the co-delivery of enzyme cascade to bloodstream. In this part, we combined the strategy of coacervate complex with in situ polymerization to encapsulate enzyme cascade in a coacervate nanoreactor with crosslinked zwitterionic shell. Such structure and surface property enhanced the overall catalytic efficacy, elimination of reaction intermediates, enzymatic stability, and prolonged circulation time of the enzyme cascade, providing a protein delivery platform for enzyme replacement therapy.

2. Realize the systemic delivery of intracellularly functional protein to tumor. In this part, we combined the strategy of "stealth" surface with cell-permeable nanocapsule to construct a nanocomplex with a PMPC shell. The nanocomplex facilitated overcome the biological barriers of immune clearance, tumor accumulation and penetration, cellular internalization, and endosomal escape, displaying an effective tumor inhibition.

Overall, this dissertation utilized various strategies and developed novel protein delivery platforms for overcoming biological barriers and improving the bioavailability of protein therapeutics, which broadens their applications.

The dissertation of Jie Ren is approved

Yi Tang

Dante Simonetti

Stephanie Seidlits

Yunfeng Lu, Committee Chair

University of California, Los Angeles

2020

Table of Contents

List of Figures

Acknowledgement

To my mentor professor Yunfeng Lu, my dissertation committee members, my lab mates who have helped me in 4-year Ph.D. program. because I owe it all to you. Many Thanks!

I am so grateful that I have such a great opportunity to do a doctorate and spent my last four years to learn how to think as a researcher. I would like to thank all the people who supported me during my Ph.D. study.

Foremost, I would like to thank my mentor Professor Yunfeng Lu for his supervision, patience and encouragement throughout my research. He teaches me how to do the research, how to always think about something big. He teaches me how to deal with the difficulties encountered in the research process and always encourages me.

I would like to thank my dissertation committee members, Professor Yi Tang, Professor Dante Simonetti, and Professor Stephanie Seidlits for their guidance and help with my research and dissertation.

I would like to express my appreciation of Dr. Yang Liu, Dr. Jie Li, and Dr. Chaoyong Liu for their guidance of research as senior members in Lu Lab. And I would like to thank Dr. Di Wu and Ran Yan who collaborate with me in the animal experiments. I appreciated Dr. Jing Wen for her great help on reagents and materials. I also would like to thank Dr. Meng Qin, Professor Masakazu Kamata and Professor Irvin Chen for the excellent collaboration.

And I would like to take this opportunity to thank all Lu group members and summer students for their helpful discussion and support.

Vita

Education

09/2006-06/2010 **B.S.** Nankai University

School of Chemistry

Research Experiences

09/2010-06/2016 **Ph.D.**

Department of Polymer Chemistry, Nankai University

Supervisor: Dr. Linqi Shi

10/2013-10/2015 **Exchange Student**

Department of Chemical and Biomolecular Engineering, UCLA

Supervisor: Dr. Yunfeng Lu

09/2016-present **Ph.D. Candidate**

Department of Chemical and Biomolecular Engineering, UCLA

Supervisor: Dr. Yunfeng Lu

Publications

2020 Coacervate-based nanoreactor as a universal platform for enzyme cascade delivery. Manuscript in preparation

2020 Systemic protein delivery based on sheddable PMPC-conjugated nanocomplex for the treatment of solid tumor. Manuscript in preparation

2019 D. Xu; D. Wu; M. Qin; L. R. Nih; C. Liu; Z. Cao; **J. Ren**; X. Chen; Z.He; W. Yu, Efficient Delivery of Nerve Growth Factors to the Central System for Neural Regeneration. *Adv. Mater.* 2019, *31* (33), 1900727.

2019 D. Wu; M. Qin; D. Xu; L. Wang; C. Liu; **J. Ren**; G. Zhou; C. Chen; F. Yang; Y. Li, A Bioinspired Platform for Effective Delivery of Protein Therapeutics to the Central Nervous System. *Adv. Mater.* 2019, *31* (18), 1807557.

2013 **J. Ren**; Y. Zhang; J. Zhang; H. Gao; G. Liu; R. Ma; Y. An; D. Kong; L. Shi, pH/sugar dual responsive core-cross-linked PIC micelles for enhanced intracellular protein delivery. Biomacromolecules 2013, 14 (10), 3434-3443.

2013 G. Liu; R. Ma; **J. Ren**; Z. Li; H. Zhang; Z. Zhang; Y. An; L. Shi, A glucose-responsive complex polymeric micelle enabling repeated on–off release and insulin protection. Soft Matter 2013, 9 (5), 1636-1644.

Chapter 1 The background information of protein therapeutic delivery

1.1 Protein therapeutics

Proteins are essential for living organisms, mediating almost every biological activity in nature. It has been reported that there are estimated 1 to 3 billion proteins in the human cell, which are expressed from 25,000–40,000 different genes in the human genome[1]. Proteins catalyze biochemical reactions, forming receptors, channels, and transporters in the membranes, providing intracellular and extracellular scaffolding support, and acting as biological signals to trigger pathways[2-4]. On one hand, the abundancy, diversity, and dynamicity of proteins make the human body vulnerable to pathogens that defunctionalize or down-regulate functional proteins, leading to various protein-related diseases[5-7]. For example, metabolic diseases such as diabetes[8-9] and lysosomal storage diseases[10-11] are caused by the abnormal level of certain signaling proteins or enzymes. One the other hand, the advantages of proteins over small-molecule drugs endow them with great potential in clinical applications. First, proteins possess high specificity and efficiency in biological processes unparalleled by their small-molecule counterparts, leading to less interference to the irrelevant biological processes and less side effects. Second, the proteins usually serve as complex set with complementary and synergic functions, which is difficult to be simulated by small-molecule drugs. Third, most of the protein therapeutics are derived from the human source, making them well tolerated and elicit less immune response. Those advantages have directed the pharmaceutic to the development of protein-based therapeutics. The market size of protein therapeutics has increased to more than 140 billion US dollars by 2016 with 239 peptide-

based drugs and 380 drug variants approved by FDA[12]. Meanwhile, over 240 clinical trials on the newly developed protein therapeutics are ongoing now. In the academic area, more than 20000 articles and patents are published per year.

The protein therapeutics can be classified into three categories based on their functions, which are enzymes and signaling proteins, targeting proteins, and protein vaccines. Enzymes perform catalytical functions in biological reactions in the living organism while the signaling proteins up or down regulate the expression level of enzymes. As for the diseases caused by the deficiency or abnormality of enzymes or signaling proteins in pathways, the therapeutic proteins derived from endogenous sources are able to replace their deficient counterparts and restore the functions in the pathway[13-17]. It has been well exemplified by insulin that can bind to the insulin receptors on the cell membrane and regulate the glucose metabolism for the treatment of diabetes[18]. For those diseases caused by the excessive metabolic waste and overwhelming of the corresponding enzymes, the administration of exogenous enzymes can help boost the metabolic reaction and accelerate the removal of excessive metabolites.

Targeting proteins are represented by monoclonal antibodies. Most of the therapeutic antibodies are fused with humanized Fc domains so that they can simulate the human antibody and minimize the immunogenicity[19]. The versatilely engineered Fab domain provides a strong binding affinity between the antibody and antigen, triggering the subsequent pathways[20]. By far, various antibodies have been approved by FDA and employed for the treatment of cancer[21], auto-immune diseases[22], inflammatory diseases[23], infectious diseases[24] and so forth[25]. Antibodies can also serve as scavengers against the infectious pathogens by binding to the soluble molecule for destruction because the immune cells can recognize the Fc region, endocytose the attached molecule and break

down the molecule chemically and enzymatically[26]. Especially in oncology, the antigen recognition sites of immunoglobulin molecules guide the immune system to destroy targeted tumor cells, as exemplified by trastuzumab. Alternatively, antibodies are able to activate the suppressed immune cells by blocking the immune check points, as exemplified by PD-1 or PD-L1 inhibitor Nivolumab[27] and Atezolizumab[28], respectively.

Another type of therapeutic proteins is the vaccine. To develop effective immunity against foreign organisms or cancer cells, immune cells must be activated. Immune-cell activation is mediated by antigen-presenting cells, which display specific oligopeptides on the cell membrane that are derived from proteins found in foreign organisms or cancer cells. In this context, proteins that can be used as vaccines should be able to stimulate the specific receptors on the surface of antigen-presenting cells and activate the immune response, as widely demonstrated by ovalbumin[29]. Vaccines can also protect human bodies against infectious diseases or toxins. One successful example is the hepatitis B vaccine[30-31], which was created by producing recombinant hepatitis B surface antigen (HBsAg) protein. Vaccines can also be employed for the treatment of auto-immune diseases. For example, a pregnant woman may occasionally reject a fetus after she has been immunized against certain antigens carried by a fetus from a previous pregnancy. Administration of an anti-Rhesus D antigen Ig is able to prevent the sensitization of an Rh-negative mother at the time of delivery of an Rh-positive neonate[32].

Despite the great potential of proteins as candidates for the treatment of various diseases, their clinical applications are still very limited due to their undesirable natures. The biological barrier existing in the human body prevents the protein therapeutics from exerting their functions in the target sites. In next section, those biological barriers will be introduced for understanding.

1.2 biological barriers for protein delivery

Once being administrated in vivo, protein therapeutics encounter different physiological environments, in which they may be removed or disrupted, leading to compromised functions (Figure 1-1). Proteins in the free form have some unfavorable pharmaceutical properties. First, some of the protein molecules are so small (< 60 kD) that they are often rapidly eliminated from the circulation by renal filtration[33]. Second, the exogenous proteins are readily to be opsonized and removed by scavenger cells in the bloodstream or immune organs like liver and spleen[34]. Third, the fragile nature of proteins makes them vulnerable to proteolysis by the proteases[35]. Fourth, they cannot spontaneously pass biological barriers such as lipid membranes of cells due to their impermeable feature[36]. Owing to those barriers, the inability of protein therapeutics to reach the target site and exert their functions has been considered as the most critical limitation for their clinical applications, which emphasizes the importance of developing appropriate strategies for protein delivery.

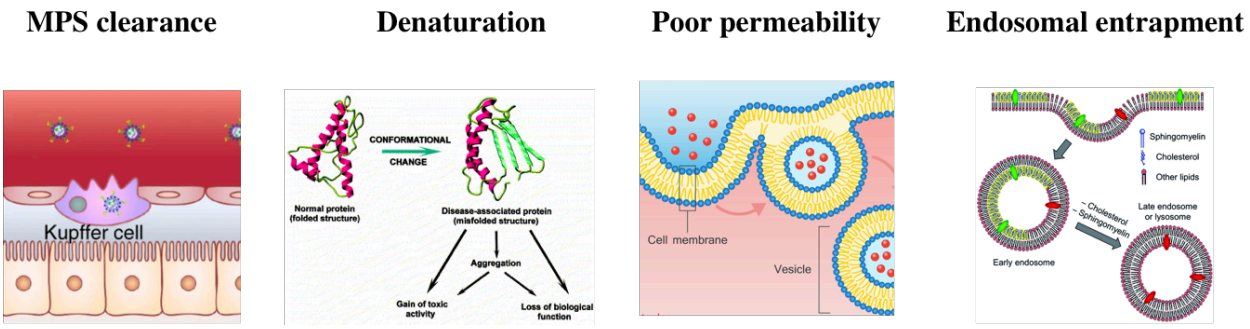

Figure 1-1 Illustration of biological barriers in the delivery process of protein therapeutics.

1.2.1 mononuclear phagocytic system clearance

Mononuclear phagocytic system (MPS) is a part of the immune system that consists of phagocytic cells located in reticular connective tissue[37]. Those cells are primarily monocytes and macrophages, which accumulate in lymph nodes and spleen[38] and sequester the drugs immediately after systematic administration. Such a process can be divided into two categories: opsonization and phagocytosis.

Once being injected to the bloodstream, the foreign proteins with amphiphilic and electrostatic surface induce non-specific interactions including Van Waals, electrostatic, and hydrophobic interactions with the serum proteins such as complement components, immunoglobulins, serum albumins, and apolipoproteins in the blood vessel[39-40]. In addition, antibodies can bind to them through specific interactions that recognize the specific antigenic determinants on the surface of exogenous proteins [41]. Such attachment by proteinaceous molecules to the exogenous proteins in the bloodstream are called opsonization.

Through the opsonization process, the attached proteins provide targets for the specialized receptors on the membrane of the phagocytic cells, facilitating the subsequent phagocytosis to digest and remove the injected foreign proteins[42]. The phagocytosis results in a fast removal of administrated protein therapeutics, leading to the short circulation and preventing them from reaching the target site where they can exert functions[43].

1.2.2 Cellular entry and endosomal entrapment

The intracellular milieu is physically segregated from the environment by the plasma membrane, which is an elastic lipid bilayer embedded with domains of lipids, carbohydrates, and membrane proteins[44]. Some small molecules like oxygen and carbon dioxide can penetrate through the cell membrane via a free diffusion mechanism. While other small molecules like nutrients and ions can be transported through the membrane by specific transporters. Whereas the lipophilic nature of the lipid composed membranes restricts the direct cellular entry of most macromolecules like proteins and genes[45].

Even if the protein can be taken up by cells through modification of cellular penetrating enhancer like TAT or being encapsulated by nanoparticles, the internalization is usually through the endocytic pathway[46]. In such a pathway, the internalized macromolecules or nanoparticles will be firstly engulfed by vesicles formed by the cell membrane. Subsequently, the vesicles mature into late endosome and lysosome, in which massive proteases could digest the proteins into small pieces and deteriorate their functions[47]. Moreover, the exocytosis pathway excretes the exosomes and removes the internalized proteins into extracellular area[48].

Besides those protein therapeutics that target the vascular compartment or extracellular areas, the intracellular pathways provide great potentials for protein-based therapy. Thus, it is of vital importance for those protein therapeutics to be effectively internalized by cells and reach the targets inside cytoplasm or other specific organelles, such as lysosomes, mitochondria or endoplasmic reticulum.

1.2.3 Protein stability

Proteins are such complicated macromolecules that even a small change in the sequence or conformation would lead to irreversible deterioration of their activity[49]. The majority of proteins have poor stability and prone to be deactivated when they are encountered with the environments different from their normal ones like non-neutral pH values[50], high temperatures[51], high salt concentration[52], proteases[53] and detergents[54].

In the bloodstream, physiological temperature (37 ^{o}C) and ionic concentration (154 mM) are usually higher than the conditions that are ideal to preserve the protein structure and activity. The blood flow in the vessel created shear forces[55] while the exogenous proteins are preferably to form aggregates with the serum proteins. Those conditions collectively could lead to the unfolding or misfolding of proteins and inactivation of their functions.

In the intracellular space, the conditions are usually harsher than those in the extracellular area. In the cytoplasm, the intracellular proteins are highly concentrated to create the macromolecular crowded environment, which could lead to the reduced native state stability of protein therapeutics due to the intense protein-protein interactions[56]. While in the late endosome and lysosome, excessive proteases as well as the acidic pH value could result in the proteolysis or hydrolysis of the protein sequences, leading to the fragmentation and dysfunction of proteins[57].

In addition, the harsh conditions in the preparation, handling, storage, and transportation process of the protein therapeutics such as long-term storage, lyophilization could also destroy the protein structure and function[58].

Thus, to effectively protect the protein functions against those conditions is one of the most important requirements for protein delivery.

1.3 Strategies for protein delivery based on nanotechnology

Although last decade has witnessed the great progress in protein engineering to alter the protein properties and realize their potentials in therapeutic applications, it is still very limited to use such a technology for protein delivery due to the difficulty in design, modification, and high cost.

In this context, nanotechnology has become the most promising strategy to overcome the barriers in the delivery process of protein therapeutics.[59] The nanoparticle candidates and loading methods are illustrated in Figure 1-2. So far, dozens of nanomedicines have already been approved for clinical use, and many more are under clinical investigation. Nanoparticles that are typically in the range of 10-150 nm in size have considerable advantages as drug carriers due to their size effect and versatile surface properties[60]. Through hydrophobic, electrostatic, or other interactions, proteins can be encapsulated in or adsorbed onto those nanoparticles such as liposomes, micelles, nanogels, and inorganic nanomaterials[61]. In the delivery process, nanoparticles could: i) protect proteins from denaturation in biological environment; ii) enhance systemic circulation half-life of proteins in the bloodstream; iii) control the release behavior; and iv) target diseased tissues, cells, and intracellular compartments[59].

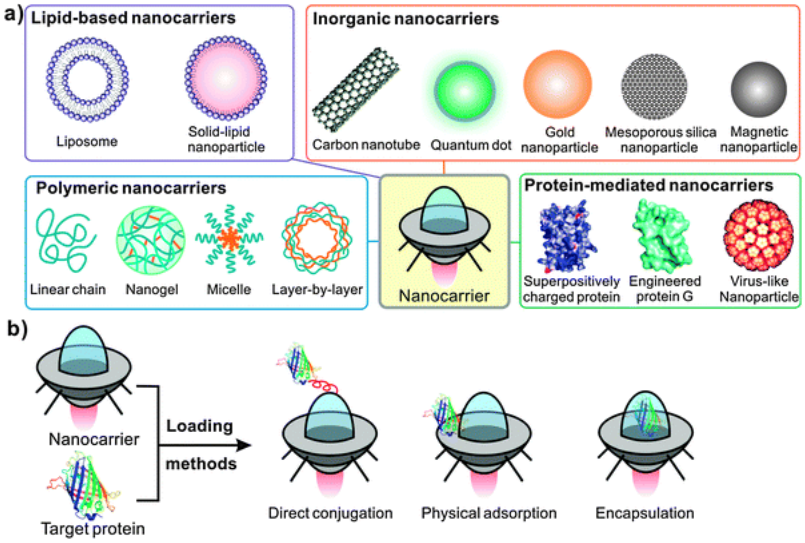

Figure 1-2 Illustration of nanoparticles and methods for protein delivery. Figure referred from refer 59.

1.3.1 Strategies to overcome immune clearance

Nowadays, "stealth" that coats the surface of nanoparticle with low-immunogenic materials has been considered as the consensus strategy in nanoparticle design. Various types of biocompatible polymers, including PHEMA[62], PVP[63], PEG[64], and so forth have been introduced to construct the nanoparticle shell. Those surface-shielding polymers can prevent the serum protein adsorption as well as the recognition of the epitopes of proteins by the immune system, and thus favorably alter their pharmacokinetics by reducing the immunogenicity and prolonging its circulation time[65]. Among those polymers, PEG is the most widely used as the decorating polymer for almost every nanomedicine in the pharmaceutical market and clinical trials.

However, PEG itself can also elicit specific antibodies in vivo, which undermines their ability to escape from immune clearance and results in the compromised pharmacokinetics. Even

in the cases of commercialized PEGylated therapeutics, the anti-PEG antibody has been found in around 20% of patients after treatment of multiple injections[66].

Recently, a novel type of polymer termed as "poly 2-methacryloyloxyethyl phosphorylcholine" (PMPC) has emerged as one of the most promising "stealth" candidates[67]. This polymer is featured by carrying both positively and negatively charged centers with an overall neutral charge in each unit, which is defined as "zwitterionic" structure. Due to this unique structure, water can be attracted and bound extensively to the polymer chain, creating a dense hydration shell surrounding them[68]. This hydration layer can effectively reduce non-specific protein adsorption and therefore confer the surface with "anti-fouling" characters. More importantly, unlike PEG, no PMPC-specified antibody has been detected in the in vivo tests, eliminating the possibility of undesired pharmacokinetic performance in multiple injections. Thus, it could be used as the "stealth" material for the construction of protein encapsulated nanoparticles.

1.3.2 Strategies for intracellular delivery

Nanoparticles have been extensively demonstrated to improve the permeability of proteins thanks to their optimal size that is within the optimal size range of endocytosis (20-200 nm). Micelles[69], liposomes, mesoporous silica nanoparticles[70], nanogels[71] have been employed to facilitate the intracellular delivery of proteins. Moreover, modification of positively charged moieties or specific ligands could further improve the cellular internalization efficiency due to the electrostatic interactions with the negatively charged cell membrane or the ligand-receptor binding with the receptors embedding in the membrane[72].

After being internalized through endocytic pathways, the ability of endosomal escape is a critical prerequisite for the nanoparticle to deliver the protein to the cytosol target. To achieve this goal, the strategy of modifying the nanoparticle with secondary or tertiary amino contained groups that could induce the "proton sponge effect" has been widely used[73]. Once being trapped in the late endosome or lysosome, the amino groups are protonated to absorb free protons in response to the acidic endosomal or lysosomal environment (pH 4.5-7.0). As the absorbed protons accumulate, they gradually increase the membrane potential past the equilibrium level. Since this equilibrium potential is primarily established by chloride diffusion, chloride will then begin to diffuse into the endosome in an attempt to restore the equilibrium potential which raises the osmotic pressure further. This causes the endosome to swell and expand until it passes a critical area strain, rupturing the lipid bilayer membrane and releasing the entrapped nanoparticles into the cytoplasm.

1.3.3 Strategies to protect Protein stability

Encapsulating proteins into nanoparticles confines them into a limited space, in which the movement of peptide chains is restrained. Such a restriction reduces the possibility of protein misfolding induced by high temperature, shear forces, lyophilization, long-term storage, and high salt concentration[74]. Moreover, the coating shell of the nanoparticle is able to restrict the accessibility of protease to the encapsulated proteins, thus protecting the proteins from proteolysis[75]. Based on this mechanism, micelle, liposome and polymersome entrapping proteins have been utilized for protein activity protection.

Besides, the crosslinking strategy that packs the proteins within the crosslinked polymeric network further strengthens the restriction, thus providing better protection of protein activities. In

this context, nanogels with crosslinked polymeric structure have been utilized to encapsulate proteins, as represented by nanocapsule that forms by in situ polymerization on the surface of single protein[76]. For example, Jie Li et al. has reported that by wrapping the organophosphorus hydrolase with polymer network, the enzyme showed remarkable improvement in the stability against high temperature, organic solvents, proteolysis, free-thaw cycles, and long-term storage[77].

In summary, protein-based therapeutics represent the novel direction of pharmaceutical development due to their unique advantages. However, the biological barriers hamper the clinical applications of protein therapeutics, which emphasizes the need to address those barriers. Current strategies based on conventional nanoparticles usually focus on one or two barriers due to their structural limitation, whereas the unaddressed barriers lying in the administration process could lead to the compromised delivery efficacy. Thus, it is of the urgent need to develop novel delivery strategies for overcoming those barriers systemically and improving the therapeutic outcomes.

1.4 Dissertation objectives and research scope

The objective of my dissertation is to design, construct, and characterize novel types of nanoparticles, overcoming the biological barriers for protein delivery. Briefly, my dissertation is dedicated to the following aspects:

(1) Develop nanoreactor based on coacervate core and crosslinked shell structure as a platform to enable the delivery of enzyme cascade for enzyme replacement therapy.

(2) Develop sheddable Poly(2-methacryloyloxyethyl phosphorylcholine) conjugated nanocomplex to enable the systemic delivery of intracellularly functional protein therapeutics for the treatment of solid tumor.

Chapter 2 Coacervate-based nanoreactor as a universal platform for enzyme cascade delivery

2.1 Introduction

Enzyme catalyze every single biochemical reaction in nature. Despite the high efficiency, selectivity, and specificity that have been extensively proved,[78-80] the sophisticated compartmentalization endows enzymes with unparalleled complementary functions compared to their artificial catalytic counterparts. [81-82] In living organisms, enzymes are usually confined in limited space like cellular organelles to enable the close proximity among one another in the reaction cascade, affording an enhanced substrate transferring from the upstream enzyme to the downstream one, thus maximizing the overall reaction efficacy and minimizing the generation of intermediates.[83-87] In this context, the malfunction of single enzyme or multiple enzymes in the pathway leads to severe metabolic disease, such as gout,[88] lysosomal storage diseases,[89] and so forth. To restore the metabolic pathway and mitigate the diseases, the most straightforward strategy is enzyme replacement therapy, which is to administrate the corresponding enzymes to replace the missing or dysfunctional ones.[90-92]

Recently, the newly developed protein engineering technique and the revealing of metabolic pathways greatly broaden the library of enzymes that possess therapeutic potentials.[93-95] However, the clinical applications of enzymes are still limited due to their intrinsic drawbacks and biological barriers. During the synthetic, storage, and administration process, the harsh conditions encountered by enzymes such as high temperature,[96-97] freeze-thaw process,[98-99] and

protease-abundant environment[57, 100-101] lead to the denaturation of enzyme structure and function loss. Since the engineered enzymes are usually exogenous proteins that elicit immunogenicity, their quick clearance by mononuclear phagocytic system results a low circulation time and off-targeting delivery.[102-104] Moreover, in the treatment of metabolic diseases that needs to restore the functions of multiple enzymes in the pathway, administration of single type of enzyme or separately multiple enzymes usually results in low overall catalytic efficacy and the accumulation of toxic intermediates that cause severe side effects in the human body.[105-107] Therefore, it is critical to develop optimal delivery systems of therapeutic enzymes for enzyme replacement therapy.

To address those problems, nanoreactors that confine enzyme cascade in a limited space with a protective shell have been widely developed and studied. Based on the encapsulation mechanism, they can be categorified into several classes: liposome/polymersome,[108-111] inorganic nanoparticles,[112-114] nanocapsules,[115-116] and coacervate complex.[117-118] Liposome/polymersome and inorganic nanoparticle can encapsulate enzymes through hydration or physical adsorption method, protecting the enzymes from denaturation in harsh conditions.[119-121] Whereas the lack or low density of hydrophilic moieties on their surface leads to the structural instability and quick immune clearance.[122-124] Nanocapsules with crosslinked polymer network is constructed by in-situ polymerization from the surface of enzymes. The polymer network endows the encapsulated enzyme with enhanced stability and versatile surface properties, greatly improving their bioavailability.[77, 125-128] Besides the single enzyme encapsulated nanocapsules, our group have developed enzyme cascade encapsulated nanocapsules by connecting multiple enzymes through inhibitor conjugated DNA origami and subsequent polymerization and removal of the DNA crosslinker.[116] Such a structure enables close proximity among enzymes, improving the catalytic efficiency of enzyme cascade and minimizing the generation of toxic intermediates. However, the

high cost and complicated synthetic chemistry of DNA crosslinkers make it difficult to serve as a universal platform for enzyme delivery. Polyelectrolytes can condense enzyme cascade within the coacervate core to form enzyme encapsulated coacervate complex, simulating the structure of organelles in nature. Yet the weak electrostatic interaction between polymers and enzymes are readily to be screened by the physiological ionic strength, leading to the dissociation of the coacervate complex and release of the encapsulated enzymes.[129-130] In addition, the use of organic solvents or high concentration of free radicals during the encapsulation process inevitably causes activity loss of enzymes, further compromising their therapeutic outcomes.[131-133] Due to those drawbacks of nanoparticles, none of them has been employed for enzyme replacement therapy, leaving us urgent need to rationally design novel enzyme delivery platforms.

Herein, we combined the strategy of nanocapsule and coacervate complex, constructing a versatile nanoreactor with enhanced structural and enzymatic stability as well as tunable surface properties for in vivo delivery of enzyme cascade. As illustrated in Figure 2-1, we first condensed multiple enzymes with a Polyethylene glycol (PEG) and α-Bromoisobutyryl (BIB) grafted positively charged polymer polyallylamine (PEG-*g*-BPAH) into a coacervate complex. Instead of free radical polymerization employed in conventional synthesis of nanocapsules, we chose single-electron transfer living radical polymerization (SET LRP) from the pendant initiator BIBB with monomers, crosslinkers, catalyst and ligand at room temperature, leading to the formation of polymeric network growing from the initiator in the core. Given the relatively low free radical concentration, the enzyme activity is expected to be maximumly preserved. Owing to the highly concentrated enzymes in the core, close proximity amongst multiple enzymes was realized, which enables the formation of enzyme cascade with complementary effects. Meanwhile, the polymeric network is able to effectively stabilize the coacervate core as well as the enzymatic activity inside.

By regulating the monomer type and ratio in polymerization process, we can readily tune the surface charge of the nanoreactor and thus its in vivo trafficking. Furthermore, we employed uricase (UOX) and Catalase (Cat) co-encapsulated nanoreactor with anti-fouling 2-Methacryloyloxyethyl phosphorylcholine (MPC) shell as a model to evaluate its potential of the novel nanoreactor in therapeutic applications. The nanoreactor could escape from the immune clearance, prolong the circulation of enzymes in the bloodstream, reduce the blood uric acid level, and prevent the damage from the toxic intermediate generated in the catalytic process.

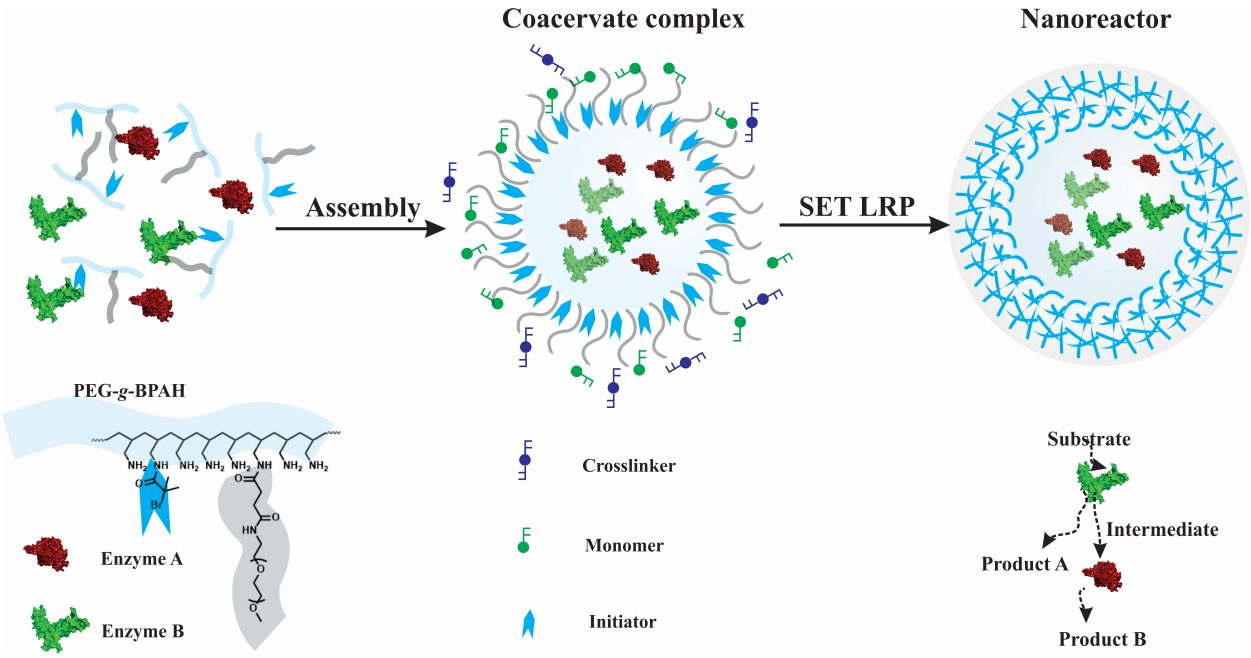

Figure 2-1 The construction procedure of enzyme cascade encapsulated nanoreactors.

2.2 Results and discussion

To verify the construction of multiple enzymes encapsulated nanoreactor, we employed UOX and Cat as the model enzyme pair. As shown in the dynamic light scattering (DLS)

measurement (Figure 2-2a), the size distribution peak at several nanometers that represents native enzymes shifted to around 100 nm after the addition of polymers, implying the condensation of the enzymes and the formation of the coacervate complex, which is denoted as P(UOX-Cat). We then conducted SET LRP with MPC as the monomer, N,N′-Methylenebis(acrylamide) (BIS) as the crosslinker from the initiators conjugated on the polymer chain to generate the UOX and Cat encapsulated nanoreactor, which is denoted as n(UOX-Cat). The size of P(UOX-Cat) increased to 120 nm after the polymerization, implying that the MPC shell formed surrounding the core and the formation of the nanoreactor. Since the surface charge determines the in vivo fate of the nanoparticles, we extended the polymerization to other monomers like neutrally charged acrylamide (AAM), poly(ethylene glycol) monomethacrylate (PEG) and positively charged 3-aminopropyl acrylamide (APM) to verify the charge tunability of the nanoreactor shell. The zeta potential test after the polymerization shows that the surface charge of the nanoreactor was consistent with the charge of the incorporated monomer (Figure 2-2b). To confirm if the coacervate core was packed by the network shell, we synthesized the nanoreactor with FITC-labeled enzymes and challenged it with the strong polyanion heparin. The agarose image (Figure 2-2c) illustrates that the enzymes were released from the nanocomplex upon the competition of heparin while the nanoreactor retained the payload enzymes, indicating that the coacervate core was strengthened by the polymer network.

Two main factors that determine the enzyme function are turnover number (Kcat) and Km. Kcat represents the catalytic rate of enzymes while Km shows the accessibility of substrate to the active center. It is essential to keep both two factors of the enzymes in the nanoreactors to maximize the enzyme functions. The harsh conditions due to the introduction of organic solvents, free radicals, heat and so forth to the synthetic process usually result in a undermined catalytic rate.

To address this issue, we selected SET LRP at room temperature over other polymerization methods since the copper ions and generated free radicals that induce damages to the enzyme structure can be both minimized to maintain the enzyme activity. We synthesized six nanoreactors with different model enzymes encapsulated. As shown in Figure 2-2d, all the six enzymes retained more than 80% of their initial Kcat values after the polymerization process, suggesting a desirable enzyme activity preserved after the construction of nanoreactors. It has been reported in many nanoreactors, especially those polymersomes, that the diffusion of substrate to the enzymes was hindered by their shells with poor permeability, leading to a dramatically increased Km value[134-135]. Accordingly, we compared the Km of enzymes before and after the polymerization process. As shown in Figure 2-2e, the Km of enzymes shows no more than 20% increase after being encapsulated in the nanoreactor, indicating that the substrates had similar accessibility to the enzymes in the nanoreactor compared with their counterparts in the bulk phase. With little change in both Kcat and Km values of enzymes after the encapsulation, we reason that this type of nanoreactor could preserve the enzyme functions and is able to be used further for encapsulating a variety of enzymes.

The far larger size of the nanoreactor compared to those of native enzymes provides the possibility that the multiple enzymes are accommodated in the limited space and located in close proximity. To demonstrate it, we synthesized the coacervate complex and nanoreactor with FITC dye label UOX and TAMRA dye labeled Cat co-encapsulated, denoted as P(FUOX-TCat) and n(FUOX-TCat), respectively. FITC and TAMRA are a pair of fluorescent donor and acceptor. To achieve a FRET effect, the distance between the two dyes must be less than 10 nm. In the fluorescent spectra (Figure 2-2f), the FITC peak decreased while the TAMRA peak increased in both P(FUOX-TCat) and n(FUOX-TCat) compared to those in the FUOX and TCat mixture,

displaying a clear FRET effect. That implies that UOX and Cat were associated closely in the coacervate core of the nanoreactor (<10 nm). It has been calculated that the enzymes in the reaction cascade have the "substrate channeling" effect when the distance between them is less than 20 nm.[136] Thus, we reason that enzyme cascade in the nanoreactor has such an effect, preventing the diffusion of intermediates to the bulk phase.

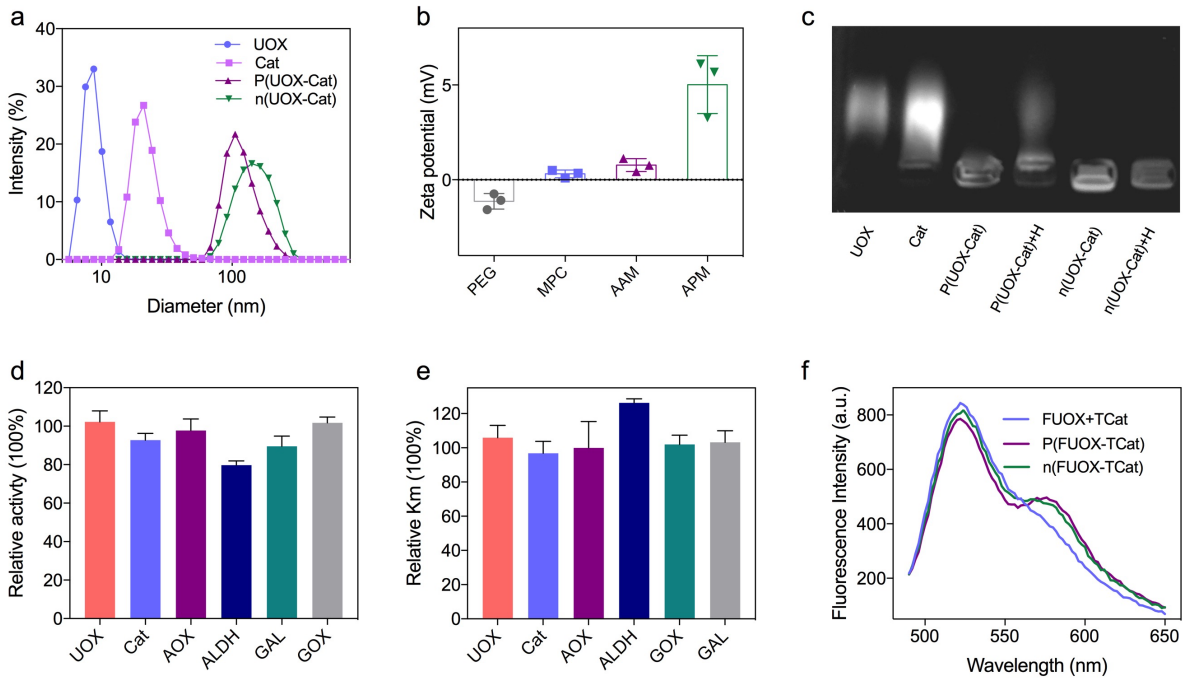

Figure 2-2 Structural characterization of the nanoreactors. (a) Size distribution of UOX, Cat, P(UOX-Cat), and n(UOX-Cat) measured by dynamic light scattering (DLS) measurement. (b) Zeta potential of n(UOX-Cat) incorporated with different monomers PEG, MPC, AAM, and APM, respectively, measured by zeta-sizer. (c) The agarose gel electrophoresis image of FITC labeled native UOX, native Cat, P(UOX-Cat), n(UOX-Cat), P(UOX-Cat) mixed with 2% Heparin, and n(UOX-Cat) mixed with 2% Heparin. Normalized Kcat (d) and (e) Km values of enzymes UOX, Cat, AOX, ALDH, GOX, GAL encapsulated in the nanoreactors after the synthetic process compared with their initial values, respectively. f) the fluorescence spectrum of the mixture of

native UOX and Cat, P(FUOX-TCat), and n(FUOX-TCat). The UOX was labeled with FITC while the Cat was labeled by TAMRA. EX: 460 nm; EM: 490-650 nm.

The limitation in intermediate diffusion facilitates the intermediate transferring from the upstream enzyme to the downstream one in the reaction cascade, improving the overall reaction efficiency. It can be exemplified by galactosidase (GAL) and glucose oxidase (GOX) enzyme pair. In the consecutive reaction, the lactose is converted to glucose and galactose by GAL and then the generated glucose is oxidized by GOX to produce H_2O_2 and glucuronic acid that can be monitored using the Amplex red assay. As illustrated in Figure 2-3a, the generation rate of the H_2O_2 was faster in the GAL/GOX co-encapsulated nanoreactors compared to that in the native enzyme mixture, showing an enhanced overall reaction efficacy. This structure also boosts the elimination of the generated intermediates. In the UOX/Cat enzyme cascade reaction, the toxic intermediates H_2O_2 generated from the oxidation of uric acid by UOX can be converted to nontoxic compound H_2O and O_2 by Cat. The generation rate of H_2O_2 by n(SOD-Cat) remarkably decreased compared with that in the enzyme mixtures (Figure 2-3b). Such enhanced elimination of intermediates was further observed in the case of three enzyme co-encapsulated nanoreactors as well. The oxidation of ethanol by alcohol oxidase (AOX) produces toxic products acetaldehyde and H_2O_2. By co-encapsulating with Cat and acetaldehyde dehydrogenase (ALDH), the generation rate of H_2O_2 and acetaldehyde both reduced significantly compared with those by the native enzyme mixtures, suggesting that this effect could be further realized in more complicated enzyme cascade systems (Figure 2-3c, d).

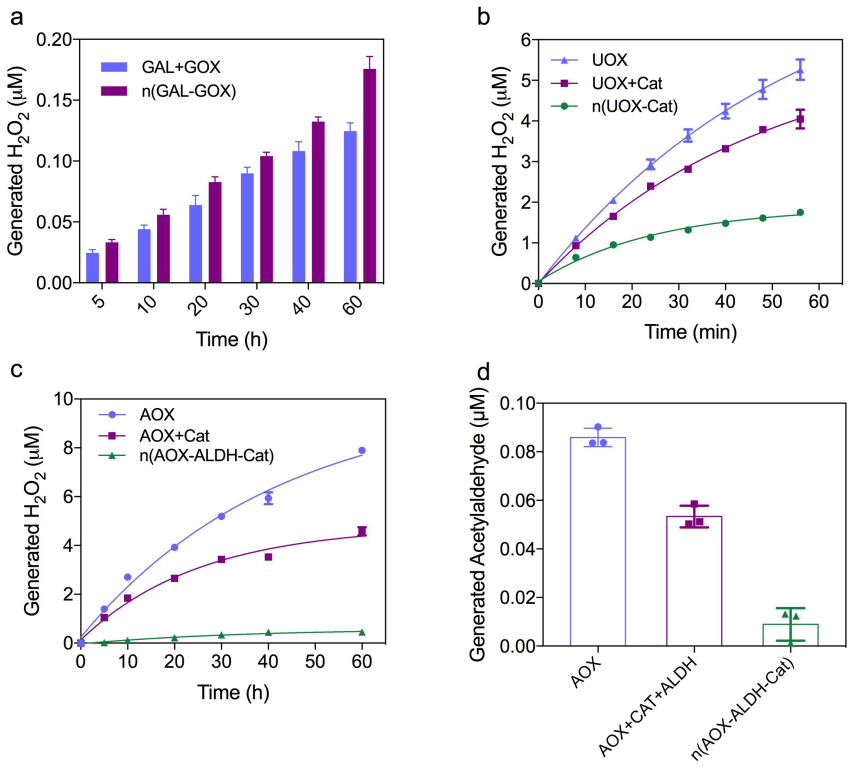

Figure 2-3 Acceleration of total reaction efficacy and elimination of intermediates. H_2O_2 generated as a function of time in (a) lactose-glucose reaction cascade catalyzed by Gal/GOX mixture or n(GAL-GOX), (b) uric acid oxidation reaction catalyzed by UOX, UOX and Cat mixture, or n(UOX-Cat), (c) ethanol oxidation reaction catalyzed by AOX, AOX/Cat mixture, or n(AOX-ALDH-Cat). (d) Acetaldehyde concentration generated in ethanol oxidation reaction catalyzed by AOX, AOX/ALDH/Cat mixture, or n(AOX-ALDH-Cat) after 1 h. Each Enzyme reaction was performed in buffers containing corresponding substrates at room temperature. The HRP and Amplex red assay was used to test the H_2O_2 concentration. The MDTH assay was used to test the acetaldehyde concentration.

The removal of toxic intermediates ameliorates their damage to the cells. First, we guaranteed the biocompatibility of nanoreactors in AML-12 cells, as demonstrated by around 100%

cell viability retained in AML-12 cells incubated with the nanoreactors (Figure 2a, b). Then we incubated the cells with nanoreactors or enzyme mixtures and the corresponding substrates for 12 h. The cells incubated with UOX/Cat encapsulated nanoreactor retained 90% of their initial viability whereas the viability of cells incubated with the enzyme mixtures decreased to 50% of their initial viability (Figure 2-4c). The reduction in cytotoxicity was also observed in the case of AOX/ALDH/Cat system thanks to the quick elimination of H_2O_2 and acetaldehyde by the nanoreactor (Figure 2-4d). Such effective protection of the cell viability against the toxic intermediates renders the nanoreactors potential to be employed as antidotes in in vivo applications.

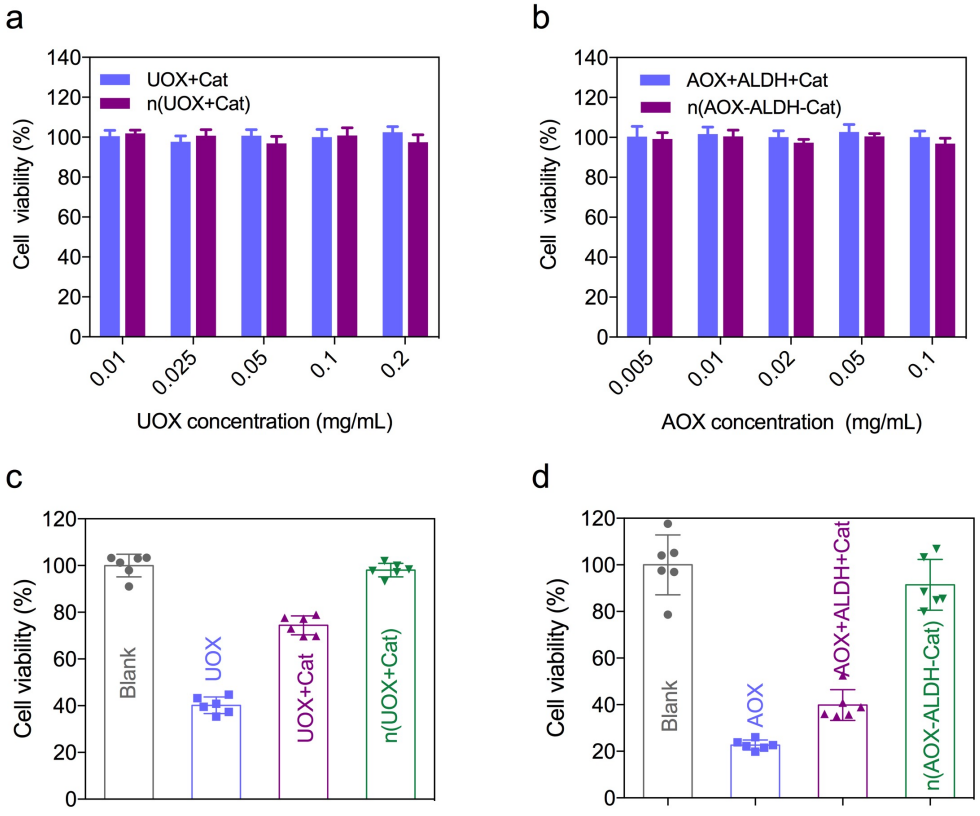

Figure 2-4 Reduction in generated intermediates protects the cell viability. Normalized cell viability of AML-12 cells after treated with mixture of UOX and Cat, and n(UOX-Cat) (a) mixture

of AOX, ALDH, and Cat, and n(AOX-ALDH-Cat) (b) for 24 h. (c) Normalized cell viability of AML-12 cells after treated with UOX, mixture of UOX and Cat, and n(UOX-Cat) for 12 h. Cells treated with PBS was set as blank. Uric acid was added to the cell medium prior to the addition of enzyme samples with the final concentration of 0.6 mM. (d) Normalized cell viability of AML-12 cells after treated with AOX, mixture of AOX, ALDH and Cat, and n(AOX-ALDH-Cat) for 4 h. Cells treated with PBS was set as blank. Ethanol was added to the cell medium prior to the addition of enzyme samples with the final concentration of 0.6 mM. The cell viability assays were performed by incubating the treated cells with 0.1 mg/mL resazurin for 2 h at 37 °C.

One of the main obstacles that enzyme encapsulated nanoparticles encounter in clinical applications is their structural instability, which results in the dissociation of the nanoparticle, release of loaded enzymes and loss of complementary functions. Thus, it is prerequisite for the nanoreactor to retain its structural stability in physiological environments. We used serum and acidic buffer to simulate the extracellular and intracellular environment, respectively, and investigated the structural stability of the nanoreactor by testing its size change with DLS measurement. The average diameter of the nanoreactor remained around 100 nm while coacervate complex swollen up to 400 nm after 24 h incubation with the bovine serum (Figure 2-5a). Similarly, the nanoreactor kept its size unchanged while coacervate complex dissociated at pH value 5.0 after 1 h incubation (Figure 2-5b). With the superior structural stability of nanoreactor in both extracellular and intracellular mimicking environments, we reason that the encapsulated enzymes are able to keep associating with one another in vivo.

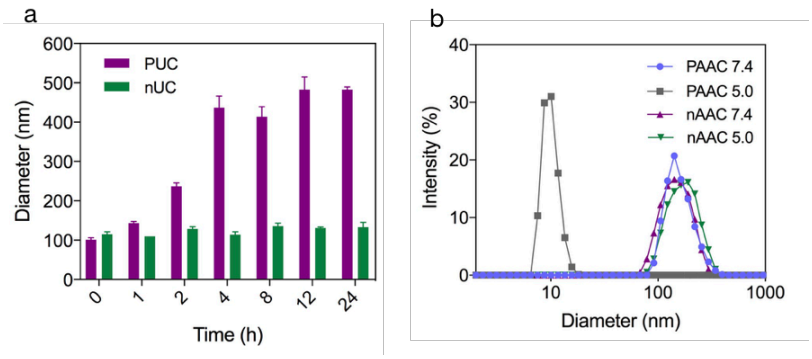

Figure 2-5 Structural stability of nanoreactors. (a) The diameter changes upon time of P(UOX-Cat) and n(UOX-Cat) incubated with 80% serum at 37 ^{o}C. (b) The change of size distribution of P(AOX-ALDH-Cat) and n(AOX-ALDH-Cat) incubated in buffers with pH value 5.0 and 7.4 at 37 ^{o}C for 1 h, respectively.

The fragility of enzymes is another main reason that leads to compromised enzyme functions in use. From the manufacturing, transportation, and storage to administration and in vivo trafficking process, enzymes encounter a variety of different conditions that can disrupt their activity. With the crosslinked topology, the polymer network is capable to restrict the access of destructive protease to enzymes and avoid the unfolding and misfolding of enzymes, thus protecting their activities against those harsh conditions. Exemplified by UOX and Cat co-encapsulated nanoreactor, UOX in the nanoreactor showed more than 90% of its initial activity after 4-week storage at room temperature while the native UOX and UOX in P(UOX-Cat) lost more 80% of their initial activity (Figure 2-6a). The enhanced enzymatic stability of UOX in the nanoreactor was also observed against the proteolysis, lyophilization, and serum incubation, showing 63%, 71%, 74% of their initial activity, respectively (Figure 2-6b, c, d). Such a capability of the nanoreactor to protect the enzymatic activity endows the enzymes with robustness to exert their optimal functions in vivo.

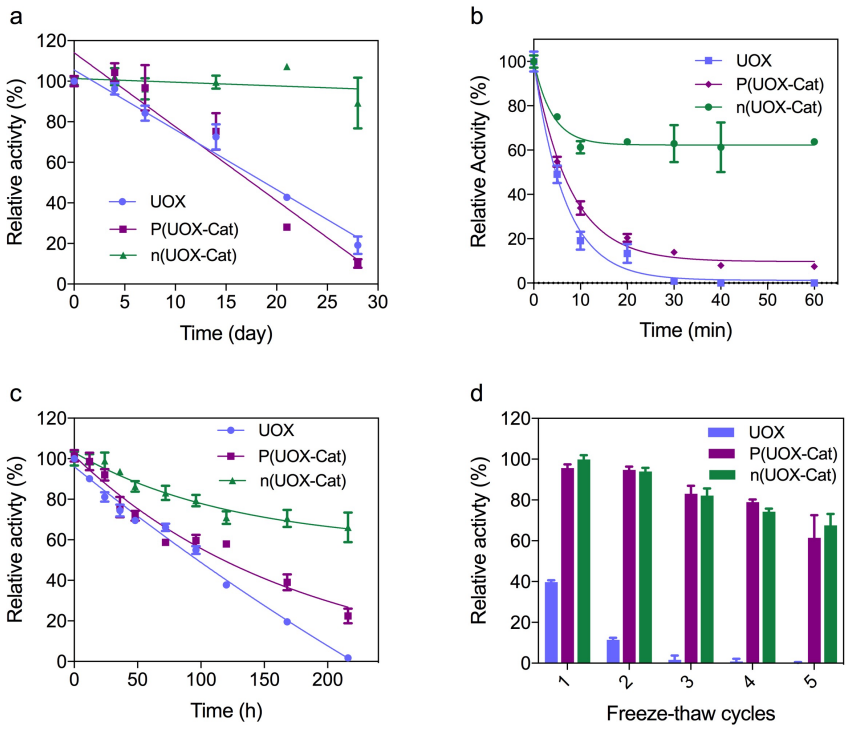

Figure 2-6 Enhanced enzymatic stability in nanoreactors. Relative UOX activity of native UOX, P(UOX-Cat), and n(UOX-Cat) as a function of time upon incubation (a) at room temperature in PBS, (b) with trypsin at the final concentration of 0.025 mg/mL at 37 ºC, (c) with 80% bovine serum at 37 ºC. (d) Relative UOX activity of native UOX, P(UOX-Cat), and n(UOX-Cat) after each freeze-thaw cycle. The activity of UOX was tested in PBS containing 0.2 mM uric acid at room temperature.

Based on the robust nanoreactor with complementary enzyme functions confirmed, we next investigated its performance as a platform for the enzyme replacement therapy using n(UOX-Cat) as a model. Uric acid is a common metabolite generated from purine metabolism. Since it can be only excreted through urine in the human body, the balance of uric acid in the bloodstream is vulnerable to be breached by the abnormally high digestion of purine contained food and the recession of kidney function, leading to hyperuricemia, subsequent gout, arthritis, disability, and

even kidney failure.[137-139] The naturally existing enzyme UOX is able to convert uric acid to allantoin that is readily excreted with high catalytic efficiency and selectivity.[140] But it is far away from practical use in the ERT due to its vulnerability to the in vivo environment as well as the toxicity brought up by the produced H_2O_2. Herein, based on the UOX and Cat co-encapsulated nanoreactor with MPC shell, we evaluated the feasibility of this platform as the antidote of uric acid.

To sustainably clear the metabolite like uric acid in the bloodstream necessitates a prolonged enzyme activity presenting in the bloodstream. While the exogenous enzymes suffer from the opsonization and clearance by the immune system, the anti-fouling polymer MPC shell could provide the capacity of escaping from the opsonization and immune clearance. In this context, we mimicked the opsonization process by incubating the nanoreactor with bovine serum at 37 ^{o}C for 2 h. After the incubation, the amount of the protein adsorbed onto the nanoreactor was similar to that in PBS while much lower than those of native proteins and P(UOX-Cat), suggesting the resistance to opsonization (Figure 2-8a). To simulate the in vivo phagocytotic clearance, we added the bovine serum pre-incubated samples FUOX and TCat mixure, P(FUOX-TCat), and n(FUOX-TCat) to the macrophage cell line J744A.1. Cat and UOX fluorescent signals inside the macrophage were much weaker in the cells treated with n(UOX-Cat) compared to those of native enzyme mixture or P(UOX-Cat), showing its resistance to phagocytosis (Figure 2-7).

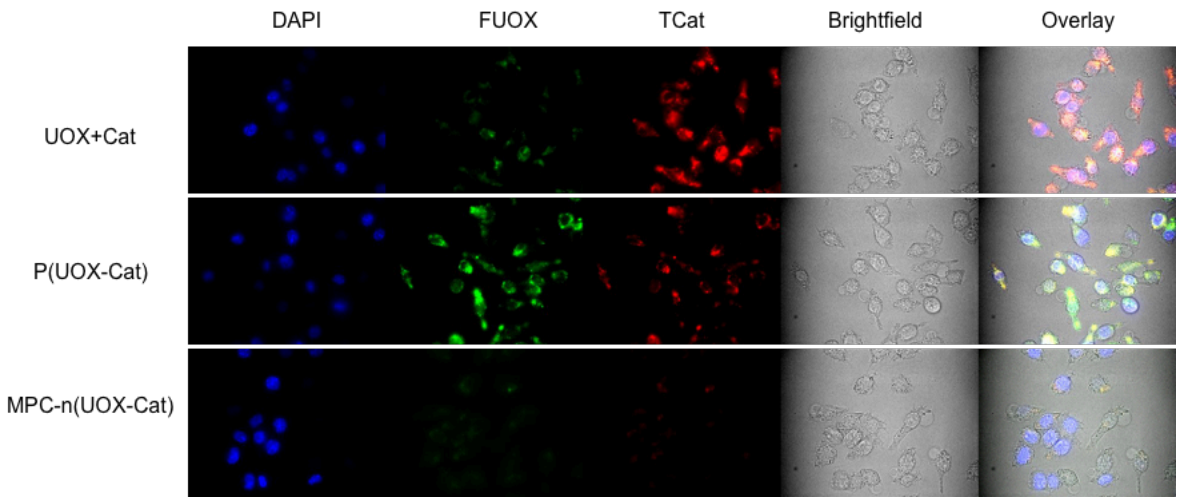

Figure 2-7 Resistance of n(UOX-Cat) to phagocytosis. Fluorescent images of J774A.1 cells after incubation with native UOX and Cat mixture, P(UOX-Cat), and n(UOX-Cat) for 4 h.

The ability of n(UOX-Cat) to escape from immune clearance in vivo was further evaluated by its organ biodistribution in mice. Alexa fluor 647 labeled UOX and n(UOX-Cat) were intravenously injected to mice (BALB/c), respectively. The organs were taken out and applied to fluorescent imaging 12 h post-injection. As observed in fluorescent images, strong signals were observed in the liver and spleen of the mice administrated by native UOX with a relative fluorescence intensity (RFI) of 12.04×10^9 and 4.37×10^9, respectively. Whereas the signals in the liver and spleen of the mice administrated by n(UOX-Cat) were both weaker with RFI of 7.29×10^9 and 2.46×10^9 comparably, implying its reduced accumulation in RES organs (Figure 2-8c, d).

Given the resistance to the immune clearance and enhanced enzymatic stability, we then tested the circulating enzyme activity in the bloodstream. The mice (BALB/c) were intravenously administrated with UOX and Cat mixture, P(UOX-Cat), and n(UOX-Cat), respectively. The

pharmacokinetic profile (Figure 2-8b) shows that the UOX activity in the serum of the mice injected with n(UOX-Cat) had a half-life of 21.2 h, which was much longer than those of native UOX and P(UOX-Cat) (4.0 h and 5.2 h).

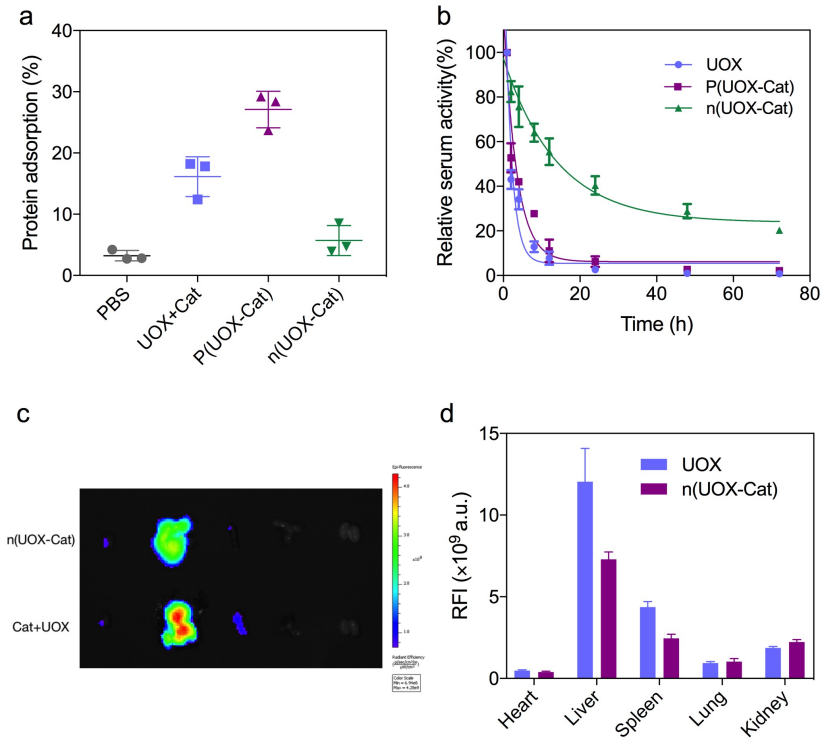

Figure 2-8 Pharmacokinetics and biodistribution of n(UOX-Cat). (a) Normalized Protein adsorption of native enzyme UOX and Cat mixture, P(UOX-Cat), and n(UOX-Cat) upon 25% bovine serum incubation for 2 h at 37 ºC. The samples were filtered and washed with 200 μL PBS for 3 times after incubation. The protein concentration was determined by BCA assay. (b) Pharmacokinetic profiles of mice after intravenous injection of native UOX, P(UOX-Cat) or n(UOX-Cat). The dosage was 10 U/kg corresponding to the UOX activity. Mean ± s.e.m., n = 3. (c) Ex *vivo* images of dissected tissues including heart, liver, spleen, lung, and, kidney the mice administered with n(647UOX-Cat). The mice were perfused with PBS and organs were harvested 12 h post-intravenous injection. (d) The relative fluorescence intensity of Alexa fluor 647 labeled

native UOX and n(UOX-Cat) in heart, liver, spleen, lung, and kidney of mice (BALB/C) 12 h post-injection.

With the long-term retainment of the blood enzymatic activity, we then evaluated the ability of n(UOX-Cat) to reduce the blood uric acid and the generated H_2O_2 in mice. The blood uric acid level of the mice treated with native and P(UOX-Cat) reduced to around 130 μM 24 h post-injection and quickly rebounded to the normal level after 72 h. Whereas the blood uric acid level in the mice upon injection of n(UOX-Cat) declined to around 100 μM and kept that level up to 120 h, suggesting a superior capability of reducing the blood uric acid level by the long-term circulated nanoreactor in the bloodstream (Figure 2-9a). Furthermore, the in vivo toxicity of n(UOX–Cat) was investigated by measuring the level of lactate dehydrogenases (LDH) in serum. The leakage of intracellular LDH to the serum indicates the abnormal cell apoptosis due to the accumulation of H_2O_2. As shown in Figure 2-9b, the LDH level of mice injected with n(UOX-Cat) (0.934 U/mL) was close to those treated with PBS (0.814U/mL), which were significantly lower than those treated with the mixture of n(UOX) and n(Cat) (1.28 U/mL), and n(UOX) (1.59 U/mL). Thus, the acceleration of blood uric acid degradation as well as the prevention of H_2O_2 damage provides the potential that the n(UOX-Cat) can be used as the long-term antidote for the treatment of hyperuricemia.

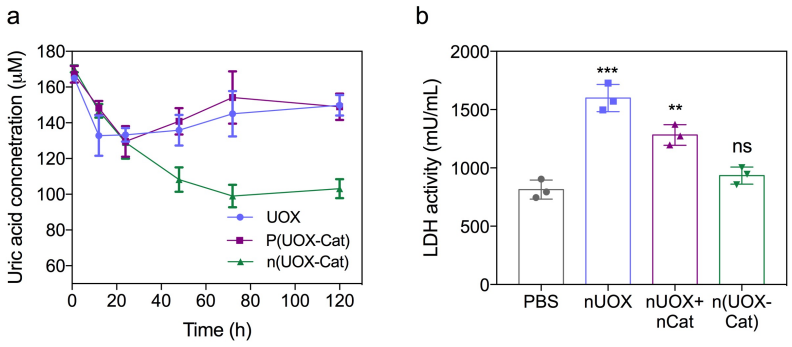

Figure 2-9 Uric acid reduction and biocompatibility of n(UOX-Cat). (a) Blood uric acid level as a function of time in mice after intravenous injection of native UOX, P(UOX-Cat) or n(UOX-Cat). (b) Blood LDH activity level in mice 24 h after intravenous injection of nUOX, n(UOX) and n(Cat) mixture, and n(UOX-Cat). mice injected by PBS was used as the control. The dosage of UOX was 10 U/kg while the Cat was 4000 U/kg. Mean ± s.e.m., n = 3.

2.3 Conclusion

In summary, we have demonstrated a design for enzyme encapsulated nanoreactor with highly preserved enzyme activity, substrate accessibility, and complementary functions in the cascade reactions. The nanoreactor enables enhanced enzymatic and structural robustness, and tunable surface properties. UOX and Cat co-encapsulated nanoreactor shows an enhanced blood circulation and capability of reducing the uric acid level in vivo. Considering the vast library of enzymes with various functions, such a nanoreactor can be employed as a promising carrier to deliver enzyme cascade for the treatment of metabolic diseases, broadening the use of enzyme-based therapies.

Since different enzymes in the reaction cascade have different turnover numbers, the overall reaction rate could be highly dependent on the molar ratio of the enzymes in the nanoreactor. In the future, we will optimize the ratio of the enzymes to reach a maximized overall reaction rate. Moreover, since all the oxidative enzymes are limited in clinical applications due the toxic byproducts H_2O_2, we plan to extent the application from hyperuricemia to other oxidative enzyme related diseases with the platform.

2.4 Experimental section

2.4.1 Materials

UOX, Nicotinamide adenine dinucleotide (NAD+), trypsin, and horse radish peroxide (HRP) were purchased from Calzyme Inc. PAH, 2-Bromoisobutanoic acid N-hydroxysuccinimide ester (BIB-NHS), GOX, GAL, Cat, ALDH, AOX, AAM, MPC, and 3-methyl-2-benzothiazolinone hydrazone hydrochloride hydrate (MBTH) were purchased from Sigma Aldrich Inc. CuBr, Me6TREN, acetaldehyde, 2-mercaptoethanol, ortho-Nitrophenyl-β-galactoside (ONPG), H_2O_2, Amplex red and BCA assay kit were purchased from Thermofisher Inc. PEG-NHS was purchased from Creativepegwork Inc. TAMRA-NHS, FITC-NHS, and Alexa fluor 647-NHS, Hoechst were purchased from Fluoroprobes Inc. Buffers are prepared following the methods depicted in the previous work. J774A.1 and AML-12 cells were purchased from American Type Culture Collection (ATCC). The Dulbecco's Modified Eagle Medium (DMEM) growth medium, trypsin and Fetal Bovine Serum (FBS) was obtained from Corning.

2.4.2 Instruments

Uv adsorption, fluorescent intensity and spectra were recorded with a Tecan Infinite 200 PRO plate reader. 1H NMR spectra were recorded with a Bruker AV400 broad band FT NMR spectrometer. The kinetic of H_2O_2 degradation were recorded with a Beckman-Coulter DU730 at the wavelength of 240 nm. Dynamic light scattering (DLS) studies of the enzyme nanocomplexes was measured on Zetasizer Nano instrument (Malvern Instruments Ltd., Kingdom). Transmission electron microscope (TEM) images were obtained on T12 Quick CryoEM and CryoET (FEI). The fluorescence microscope images were acquired by Leica dmi8 inverted microscope. The Confocal microscope images were obtained by Confocal SP8-STED/FLIM/FCS. The optical imaging and quantification were achieved by IVIS Lumina II (Perkin Elmer).

2.4.3 Synthesis of PEG-g-BPAH

100 mg PAH (Mw: 17000) was dissolved into 1 mL HEPES buffer (pH 8.0, 500 mM), followed by the addition of 100 mg PEG-NHS (Mw: 5000). The mixture was allowed to incubate at R.T. for 2 h. Then 20 mg BIB-NHS was dissolved into 200 μL DMSO and added in, incubating at R.T. for another 2 h. The solution was dialyzed against DI water for 24 h to remove the unconjugated PEG-NHS and BIB-NHS (Mw cutoff: 12KD). The purified polymer solution was then lyophilized to obtain a white powder, which was re-dissolved into D_2O and tested with ^{1}H-NMR.

2.4.4 Synthesis of one-enzyme encapsulated coacervate complexes

The one-enzyme encapsulated coacervate complexes were obtained by condensing the corresponding enzyme with the positively charged polymer. Briefly, the enzyme and PAH-*g*-BPEG were both dissolved into HEPES buffer (50 mM, pH 7.4) at the concentration of 1 mg/mL, respectively. Then the enzyme solution was mixed with polymer solution and incubated at R.T. for 15 min. The mass ratios of UOX, Cat, AOX, ALDH, GOX, and GAL to the polymer were set to 5:1, 10:1, 5:1, 2.5:1, 2:1, and 5:1, respectively. Then the uncondensed enzymes were removed by passing through the DEAE column with HEPES buffer (50 mM, pH 7.4) as the eluent buffer. The obtained coacervate complexes were stored at 4 ^{o}C for further use.

2.4.5 Synthesis of multiple-enzyme cascade encapsulated coacervate complexes

The synthetic protocol of multiple-enzyme cascade encapsulated coacervate complexes were similar to that of one-enzyme encapsulated ones. Cat and UOX solution were first mixed with a molar ratio of 1:1, followed by the addition of polymer solution at the mass ratio between the total enzyme and polymer of 5:1. The mixture was incubated at R.T. for 15 min and purified with DEAE column. In the case GOX and GAL co-encapsulated coacervate complexes, the molar ratio between the two enzymes was set to 1:1 while the mass ratio between the total enzyme and polymer was 2.5:1. In the case of AOX, ALDH, and Cat, the molar ratio among those enzymes was 1:2.5:1 while the mass ratio between the total enzyme and polymer was set to 5:1.

The fluorescent dye labeled nanoreactors were synthesized followed the same protocol. The nanoreactor encapsulating FITC labeled UOX, TAMRA labeled Cat was denoted as n(FUOX-

TCat). The nanoreactor encapsulating FITC labeled AOX and TAMRA labeled Cat was denoted as n(FAOX-TCat). The nanoreactor encapsulating alexa fluo 647 labeled UOX and Cat was denoted as n(647UOX-Cat).

2.4.6 Synthesis of enzyme encapsulated nanoreactors

The nanoreactors were constructed through the in situ SET LRP from the BIB initiator groups in coacervate complexes. The Synthesis of n(SOD-Cat) with MPC shell followed the procedure below:

To a glass bottle fitted with a magnetic stir bar and a rubber septum, tris[2-(dimethylamino)ethyl]amine (Me6TREN, 0.11 μM) were charged and the mixture was bubbled with nitrogen for 10 min. Then 0.055 μM CuBr was added to the glass bottle under a slightly positive nitrogen atmosphere. The mixture immediately became blue (CuII) and a purple/red precipitate (Cu0) and was allowed be purged further with nitrogen for 10 min. At the same time, to another glass bottle fitted with a magnetic stir bar and a rubber septum, 1 mL coacervate complex solution (0.55 μM EBIB), MPC (1.3 mM), and BIS (0.132 mM) were charged. The mixture was bubbled with nitrogen for 20 min. After then, the degassed monomer/initiator solution was transferred through a cannula to the glass bottle with Cu(0)/$CuBr_2$/Me6-TREN catalyst under nitrogen protection. The glass bottle was sealed and allowed to stir gently at room temperature for 15 min. The polymerization was stopped by exposure in air. The reaction mixture was dialyzed against EDTA solution (1 mM) for 24 h and subsequent DI water for another 24 h to remove the catalysts and unreacted monomer and crosslinker. The as-prepared enzyme encapsulated nanoreactor was stored as a solution at 4 ^{o}C for further test.

The synthesis of nanoreactors with other enzymes or enzyme cascades followed the similar procedure with the corresponding enzyme encapsulated coacervate complexes. The synthesis of nanoreactors with other monomers followed the similar procedure with PEG480 acrylate, AAM, or APM at the molar ratio between BIB and monomers of 1: 1200, 1:3000, 1:1000, respectively.

2.4.7 Determination of enzyme concentration

The concentration of enzyme was determined by BCA assay. BCA working solution was prepared by mixing 50 volume of Reagent A and 1 volume of Reagent B together. Standard enzyme solutions were made with corresponding native enzyme at a series of concentrations (0.05, 0.1, 0.2, 0.5, 1, 2 mg/mL). BCA assays were conducted by mixing 5 μL of standard solutions as well as the sample solution with 50 μL BCA working buffer into each plate well respectively. The well plate was then incubated at room temperature for 6 h. The adsorption at 562 nm of each well was recorded by the plate reader. The concentration of the sample solutions was calculated by comparing their absorbance at 562 nm with the standard curve established under the same condition.

2.4.8 FRET test

The UOX was labeled with FITC dye at the feed ratio of 1:2.5. Briefly, 10 μL 10 mg/mL UOX solution was added by 100 μL HEPES buffer (pH=8.0, 50 mM) and 0.8 μL 0.1% FITC-NHS DMSO solution. The mixture was allowed to incubate at room temperature for 2 h, followed by purification with zeba column. The Cat was labeled with TAMRA dye at the feed ratio of 1:5 following the similar procedure as that of UOX. Then P(FUOX-TCat) and n(FUOX-TCat) were

synthesized following the procedures same as those of P(UOX-CAT) and n(UOX-Cat), respectively. The fluorescent spectra of FUOX/TCat mixture, P(FUOX-TCat), and n(FUOX-TCat) at UOX concentration of 0.005 mg/mL were recorded from 490 nm to 650 nm by plate reader (Ex: 440 nm).

2.4.9 Activity assay of enzymes

The activity of UOX was determined by monitoring the degradation of uric acid in the oxidation process. 5 μL native UOX or UOX encapsulated nanoreactor was added to 50 μL uric acid solution (pH = 8.5, 0.1 M borate buffer, uric acid concentration: 0.06 mM). The adsorption at 290 nm was recorded by plate reader at a time interval of 10 s for 10 min. The rates of catalytic reaction were achieved by plotting the absorption at 290 nm versus time and calculating the ΔA290/min from the linear potion of the curve. The Calculation is depicted as below:

$$\frac{Units}{mg} = \frac{11 \times \Delta A290/min}{1.29 \times mg\ enzyme}$$

The activity of AOX was tested by MBTH assay. Briefly, MBTH and $FeCl_3$ were dissolved in diluted HCl solution (0.1 mol) at the concentration of 8 mg/mL and 10 mg/mL, respectively. 15 μL MBTH solution was mixed with 15 μL $FeCl_3$ while 2 μL AOX sample (0.01 mg/mL) was mixed with 13 μL ethanol solution (HEPES buffer pH 7.4, 0.2%w/v) and 15 μL MBTH solution. Both mixtures were incubated at room temperature for 15 min, followed by mixed together and tested the Uv adsorption at 630 nm by plate reader.

The activity of Catalase was determined by monitoring the decrease rate of H_2O_2 in the degradation process. 5 μL native Catalase or catalase encapsulated nanoreactor (0.02 mg/mL) was added to 250 μL H_2O_2 solution (pH = 7.4, 0.1 M HEPES buffer, H_2O_2 concentration: 0.03%w/v). The initial rates of catalytic reaction were achieved by plotting the absorption at 240 nm versus time for 2 min and calculating the ΔA240/min from the linear potion of the curve. The Calculation is depicted as below:

$$\frac{units}{mg} = \frac{51 \times \Delta A240/min}{44.6 \times mg\ enzyme}$$

The activity of ALDH sample was determined by monitoring the generation rate of NADH during the catalytic process. The assay buffer was composed by 600 mM KCl, 10 mM 2-mercaptoethanol, 20 mM NAD+, 0.16 mM acetaldehyde in HEPES buffer (100 mM, pH 8.0). 10 μL 0.25 mg/mL ALDH sample was added to 240 μL assay buffer. The initial rates of catalytic reaction were achieved by plotting the absorption at 340 nm versus time for 2 min and calculating the ΔA340/min from the linear potion of the curve. The Calculation is depicted as below:

$$\frac{units}{mg} = \frac{25 \times \Delta A340/min}{6.22 \times mg\ enzyme}$$

The activity of GAL sample was determined using ONPG assay. The assay buffer was prepared by 1 mM $MgCl_2$, 50 mM 2-mercaptoethanol, and 0.6 mg/mL ONPG in HEPES buffer (100 mM, pH 7.4). 5 μL GAL sample was added to 50 μL assay buffer. The initial rates of catalytic reaction were achieved by plotting the absorption at 420 nm versus time for 2 min using plate

reader and calculating the ΔA420/min from the linear potion of the curve. The Calculation is depicted as below:

$$\frac{units}{mg} = \frac{11 \times \Delta A420/min}{4.5 \times mg\ enzyme}$$

The activity of GOX sample was determined by the increasing rate of H_2O_2. The assay buffer was prepared by 10 mg/mL glucose, 0.1 mg/mL Amplex red, and 0.01 mg/mL HRP in HEPES buffer (100 mM, pH 7.4). 2 μL GOX sample was added to 50 μL assay buffer and allowed to incubate at R.T. for 15 min. The fluorescent signal was recorded at 590 nm (Ex: 550 nm).

2.4.10. Kinetic studies of H_2O_2 generation and elimination

The kinetic study of H_2O_2 generation was evaluated with the following procedure. D-glucose was dissolved in PBS buffer at concentration of 0.1 mg/mL; then 10 μL Amplex red solution (10% w/v in DMSO) and 2 μL HRP stock solution (1 mg/mL in PBS) were added to obtain final concentrations of Amplex red at 0.5 mg/mL and HRP at 1 μg/mL. The working solution was split into aliquots of 50 μL and added to multiple wells of 96-well plate. The mixture of native GOX and GAL, or n(GOX-GAL) was then added respectively to the working solution at a final GAL concentration of 0.1 μg/mL. The fluorescence signal (ex: 540 nm, em: 590 nm) was recorded by plate reader after 5, 10, 20, 30, 40, and 60 min (3 aliquots per time point).

The kinetic study of H_2O_2 generation was evaluated following similar procedure. As for native UOX, the mixture of UOX and Cat, and n(UOX-Cat), the substrate in the working solution was changed to uric acid at concentration of 0.1 mg/mL. For native AOX, the mixture of AOX

and Cat, and n(AOX-ALDH-Cat), the substrate in the working solution was changed to ethanol at concentration of 1 mg/mL.

2.4.11 Study of acetaldehyde elimination

The acetaldehyde elimination was tested by MBTH assay. Briefly, 2 μL native AOX, the mixture of AOX and ALDH, and n(AOX-ALDH-Cat) (0.01 mg/mL) was mixed with 13 μL ethanol solution (ALDH assay buffer, 2 mg/mL) and incubated for 1 h at room temperature, followed by mixing with 15 μL MBTH solution. Meanwhile, 15 μL MBTH solution was mixed with 15 μL $FeCl_3$ solution. Both mixtures were incubated at R.T. for 15 min, followed by mixed together and tested the Uv adsorption at 630 nm using the plate reader.

2.4.12. Structural stability test

To evaluate their structural stability in extracellular environment, n(UOX-Cat) and P(UOX-Cat) were mixed with 80% serum at concentration of 2 mg/mL and incubated at 37 ^{o}C, respectively. The diameter of n(UOX-Cat) and P(UOX-Cat) was tested using DLS measurement at each time point (0, 1, 2, 4, 8, 12, 24 h). For the structural stability test in intracellular environment, n(UOX-Cat) and P(UOX-Cat) were added to Acetate buffer (150 mM, pH 5.0) at concentration of 2 mg/mL and incubated at 37 ^{o}C for 1 h, respectively. Then the size distribution of n(UOX-Cat) and P(UOX-Cat) was tested using DLS measurement.

2.4.13 Enzymatic stability test of Uricase

The enzymatic stability of native UOX, P(UOX-Cat), and n(UOX-Cat) in serum was determined following the method below: the samples (0.1 mg/mL, PBS buffer) were added to bovine serum (volume ratio 1:4) and incubated at 37 ^{o}C for certain periods (0, 12, 24, 36, 48, 72, 96, 120, 168, 216 h), followed by being stored in fridge. UOX activity assays were then performed with these samples to determine the residual activities.

The enzymatic stability of native UOX, P(UOX-Cat), and n(UOX-Cat) against proteolysis was conducted following method below: the samples (0.1 mg/mL, 10 mM borate buffer, pH 8.0, 10 mM $CaCl_2$) were mixed with trypsin stock solution (10 mg/mL) to give the final trypsin concentration to 0.025 mg/mL. Then the mixtures were incubated at 37 ^{o}C for certain periods (0, 5, 10, 20, 30, 40, 60 min), followed by being quenched in ice bath. UOX activity assays were then performed with these samples to determine the residual activities.

The enzymatic stability of native UOX, P(UOX-Cat), and n(UOX-Cat) upon long storage at room temperature was conducted following the method below: the samples (0.1 mg/mL, PBS buffer) were stored at room temperature (around 25 ^{o}C) for certain periods (0, 4, 7, 14, 21, 28 days). UOX activity assays were performed with these samples to determine the residual activities.

The enzymatic stability of native UOX, P(UOX-Cat), and n(UOX-Cat) against freeze-thaw cycles was conducted following the method below: the samples (0.1 mg/mL, PBS buffer) were added to micro-tubes. Then the tubes were immersed into liquid nitrogen for 5 min, followed by thawing in water at room temperature for 5 min. This process was conducted for five cycles for

each sample. After each cycle, UOX activity assays were performed with these samples to determine the residual activities.

2.4.14 Protein adsorption test

The relative protein adsorption of each sample was determined following the method below: 20 μL native UOX, P(UOX-Cat), and n(UOX-Cat) (1 mg/mL) were mixed with 40 μL of bovine serum and incubated at 37°C for 2 h, respectively. 20 μL PBS buffer was used as the control. After the incubation, samples were filtered and washed with 60 μL PBS for 3 times with centrifugal filtration (molecular weight cut-off, 100 kDa) to remove the unabsorbed serum proteins. After reconstituting with 60 μL of PBS, the amount of protein adsorbed was determined by measuring the overall protein concentration of each sample with BCA assay using bovine serum as the standard.

2.4.15 Cellular internalization study

We select J774.1A cell line as the model immune cell line and used the fluorescent microscope to evaluate the cellular uptake of FITC-labeled UOX (FUOX) and TAMRA-labeled Catalase (Tcat) by the cells. Briefly, J774.1A cells were seeded into a 96-well plate (5×10^3 cells/well, 100 μL/well) and cultured in Dulbecco's Modified Eagle's Medium (DMEM) (normal level of glucose in medium, with 10% FBS) for a day prior to being exposed to the samples. FUOX and TCat mixture, P(FUOX-TCat), and n(FUOX-TCat) were first incubated with 80% bovine serum for 12 h and then added to the cells (the final concentration of FUOX and TCat were set to 0.05 mg/mL and 0.1 mg/mL), respectively. Cells were further incubated for 2 h at 37 ^{o}C, followed

by washing with cold PBS for 3 times to remove the samples. Cellular uptake of each sample was observed by the fluorescent microscope.

2.4.16 Cellular viability test

Cellular viabilities upon the addition of enzyme samples were tested in AML-12 cell line. AML-12 cells were seeded into a 96-well plate (1×10^4 cells/well, 100 μL/well) and cultured in DMEM medium (normal level of glucose in medium, with 10% FBS) for 24 h, followed by the addition of native UOX, the mixture of UOX and Cat, n(UOX-Cat), n(AOx-ALDH-Cat), native AOX, and the mixture of AOX, ALDH, and Cat were added into the wells and further incubated at 37°C for 12 h, respectively. Cells added by PBS was used as control.

Cellular viabilities upon the uric acid oxidation reaction catalyzed by native UOX, the mixture of UOX and Cat, or n(UOX-Cat) were tested in AML-12 cell line. AML-12 cells were seeded into a 96-well plate (1×10^4 cells/well, 100 μL/well) and cultured in DMEM medium (normal level of glucose in medium, with 10% FBS) for 24 h, followed by the addition of uric acid solution to each well (6 mM, 10 μL). Then same amounts (0.5 mg/mL, 10 μL) of native UOX, the mixture of UOX and Cat, and n(UOX-Cat) were added into the wells and further incubated at 37°C for 12 h, respectively. Cells added by PBS were used as control.

Cell viabilities in the presence of alcohol oxidation reaction catalyzed by n(AOx-ALDH-Cat), native AOX, and the mixture of AOX, ALDH, and Cat were tested following a similar procedure. Ethanol was first added to each well at the final concentration of 0.6 mM. Then the

samples (10 μg/well) were added to each well and further incubated with the cells for 4 h, respectively. Cells added by PBS were used as control.

After the incubation, resazurin Aqueous solution (10 μL) was added into each well at the final concentration of 0.01 mg/mL and further incubated at 37 ^{o}C for 2 h. Viable cells reduced resazurin to resazufin and showed fluorescent reddish color. Quantification of the cell viability was achieved by measuring the fluorescence intensities with a plate reader (Ex = 545 nm, Em = 585 nm).

2.4.17 Pharmacokinetics study

Pharmacokinetics (PK) profiles of P(UOX-Cat), n(UOX-Cat), and native UOX were accessed by monitoring the residual UOX activity in plasma after intravenous administration. Briefly, 9 mice (BALB/c) were divided into 3 groups and intravenously injected with P(UOX-Cat), n(UOX-Cat), and native UOX via the tail vein, respectively. The injection amount of UOX samples was set to 10 U/kg. As a negative control, another 3 mice were injected with 100 μL of PBS. The blood samples (20 μL) were then taken from the tails at 1 h, 2 h, 4 h, 8 h, 12 h, 24 h, 36 h, 48 h and 72 h after the injection. The blood samples were centrifuged at 1000 rpm for 5 min to remove the blood cells. Then the UOX activity in the plasma was measured using a UOX enzyme activity assay.

2.4.18 Biodistribution test

Native UOX and n(UOX-Cat) were labeled with Alexa fluor 647 before the administration. Briefly, 0.1 mL 1 mg/mL UOX and n(UOX-Cat) were mixed with 20 μL HEPES 8.0 buffer and 1 μL 1% Alexa fluor 647 NHS ester in DMSO and allowed to incubate at R.T. for 2 h in dark, respectively. Then the mixtures were purified by zeba column and stored at 4 ^{o}C. 2 mice (BALB/c) were intravenously injected with fluorescent labeled UOX and n(UOX-Cat) via the tail vein, respectively. The injection amount of UOX samples was set to 10 U/kg. After 12 h, the mice were perfused with cold PBS, followed by the organ collection (heart, liver, spleen, lung, and kidney). The fluorescent images of each organ were recorded by the organ fluorescent imaging. The relative fluorescent intensity of each sample in the tumor was determined by ROI tools.

2.4.19 in vivo uric acid degradation

9 mice (BALB/C) were divided into 3 groups, 100 μL of native UOX, P(UOX-nCat) and n(UOX-Cat) were injected to mice via vein tail at a dosage of 10 U/kg (UOX) body weight, respectively. The blood samples (20 μL) were then taken from the tails at 1 h, 12 h, 24 h, 48 h, 72 h and 120 h after the injection. The blood samples were centrifuged at 1000 rpm for 5 min to remove the blood cells, and the concentration of uric acid in the plasma was measured using a uric acid assay kit.

2.4.20 LDH assay

12 mice (BALB/c) were divided into 4 groups, 100 μL of n(UOX), the mixture of n(UOX) and n(Cat), and n(UOX-Cat) were injected to mice via vein tail at a dosage of 10 U/kg (UOX) and 4000 U/kg (Cat) body weight, respectively. 100 μL of PBS was injected to the last group as control. The blood samples (20 μL) were then taken from the tails at 24 h after the injection. The blood samples were centrifuged at 1000 rpm for 5 min to remove the blood cells, and the LDH level in the serum was tested following the procedure described in Bergmeyer's work.[141]

Chapter 3 Systemic protein delivery based on sheddable PMPC-conjugated nanocomplex for the treatment of solid tumor

3.1 Introduction

Cancer has become the second leading death disease since last two decades. Sustainable interest has been attacked into the development of therapeutics for cancer treatment. The traditional procedure for cancer therapy mainly includes chemotherapy[142], radiotherapy[143], and surgery[144]. Unfortunately, despite the favorable therapeutic outcome in some patients, the mortality still remains high while the survival time remains short in most cases. Surgery that removes the solid tumor is the most common method for cancer treatment. Whereas the removal is usually uncertain and incomplete, which leads to tumor relapse[145]. Chemotherapy initially elicits good responses, the resistance to the chemical agents emerges during a long-term treatment[146]. Moreover, the chemotoxicity of chemotherapeutics and radiotoxicity of radiotherapy usually result in severe damage to normal cells and side effects[147]. Recently, to overcome the drawbacks of conventional therapies, researchers turn their spotlight onto the protein-based therapeutics. The sophisticated functions, specific recognition of targeting receptors, and high relevance to various pathways endows the protein therapeutics with high specificity, efficiency, and biocompatibility compared to their small-molecule counterparts.[148-150] Those advantages provoke increasing interest in the development of novel protein therapeutics for the treatment of cancer. Ever since rituximab became the first approved monoclonal antibody for the treatment of low-grade B cell lymphoma in 1997[151], protein therapeutics have dominated the new direction of tumor therapy.

According to the targeting sites where they exert functions, protein therapeutics are divided into two categories: extracellularly and intracellular functional proteins. Represented by antibodies and cytokines, extracellularly functional proteins can target the overexpressed receptors on the tumor cell, triggering certain pathways, and recruiting immune-mediated cell killing to inhibit tumor growth.[152-154] Despite their high binding efficiency, those extracellular functional proteins themselves lack cell killing mechanism, usually leading to the incomplete elimination of cancer cells, especially in the case of solid tumor.[155-158] In addition, their targeting sites are limited to overexpressed receptors on the tumor cells, which results in incompetence for those cancer types that are lack of neo-antigens, exemplified by triple-negative breast cancer.[159-160] In the contrast, the extracellularly functional proteins, represented by toxins and apoptosis-related proteins, have been widely demonstrated to possess potent capability of cell killing.[161-162] Meanwhile, the vast library of cancer-related intracellular pathways greatly broadens the spectrum of druggable targets, making them desirable alternatives or adjuvant drugs for current cancer therapeutics. However, despite their pharmaceutical potentials, none of the extracellularly functional proteins has been employed in practical applications or even clinical trials due to the challenges in systemic delivery.

Besides the biological barriers including proteolytic environment and MPS clearance that extracellular functional proteins encounter upon the administration, the delivery of intracellularly functional proteins is also hampered by their poor tumor penetration,[163-164] cellular internalization,[165] and endosomal escape.[166] To escape from the immune clearance, antifouling polymers such as PEG and PMPC have long been introduced to stealth the surface of proteins, which can prolong the circulation time and accelerate the tumor accumulation.[167-168] Whereas non-antifouling surfaces like positively charged polymers are employed to enhance the cell permeability of proteins, thus improving the cellular internalization by tumor cells.[169-170] Moreover,

to overcome other barriers like tumor penetration and endosomal escape demands surface properties of nanoparticles different from those depicted above.[171-172] The incompatibility among those feathers results in failure to address all the barriers simultaneously, which leads to compromised delivery efficiency. In this context, it is essential to rationally design dynamic delivery platform to adapt to different environments underlying in the in vivo trafficking process.

Our group has previously demonstrated a novel strategy for intracellular protein delivery based on nanocapsule technology[76]. By wrapping the protein with a positively charged and degradable polymer network via in situ polymerization, we obtained the single protein encapsulated nanocapsule. The positively charged surface and sub-30 nm size facilitate the cellular uptake of the protein by tumor cells[173]. Moreover, the amino group contained polymer shell helps the nanocapsule escape from endosome and lysosome through proton sponge effect and reach the cytoplasm after the internalization[174]. Subsequently, the degradable crosslinker incorporated in the polymer network decomposes in response to the intracellular stimuli, leading to the release of protein cargos into the cytoplasm, in which the protein eventually reaches the targeting site through intracellular trafficking[175]. Exemplified by caspase-3 and P53 that can trigger the apoptosis pathway intracellularly, we have proved that such novel delivery system is able to deliver functional protein and killing the tumor cells effectively in vitro. However, despite the breakthrough in the intracellular delivery, this system didn't address the problem of immune clearance and tumor accumulation in systemic delivery, which undermines its potential in practical applications.

To address this problem, we developed a novel nanoparticle for systemic delivery of intracellularly functional proteins based on the nanocapsule with sheddable Poly (2-

methacryloyloxyethyl phosphorylcholine) (PMPC) shell (Figure 3-1). We first synthesized positively charged nanocapsule with redox-responsive crosslinker incorporated. Then we conjugated the anti-fouling polymer PMPC onto the surface of the nanocapsule via an acidic-responsive linker. The conjugated PMPC formed a dense hydration layer surrounding the nanocapsule, endowing it with the ability of long circulation and reduced immunogenicity, as was widely reported. Once leaking into the tumor site through enhanced permeability and retention effect (EPR), the PMPC shell assisted the tumor penetration of the nanoparticle. Meanwhile, the linker connecting PMPC and nanocapsule broke down responding to the slightly acidic tumor environment (pH 6.4-7.2), exposed the positively charged surface, accelerating the cellular internalization by tumor cells. After being internalized through endocytosis, the nanocapsule could escape from the endosome and lysosome, release the protein into the cytoplasm, as demonstrated by previous work. In this work, we investigated the long circulation, tumor accumulation, tumor penetration, dynamic cellular internalization, and endosome escape of the nanoparticle with BSA as the model protein while the tumor inhibition and therapeutic outcome with ribosomal inhibitor saporin (SAP) as the model toxin.

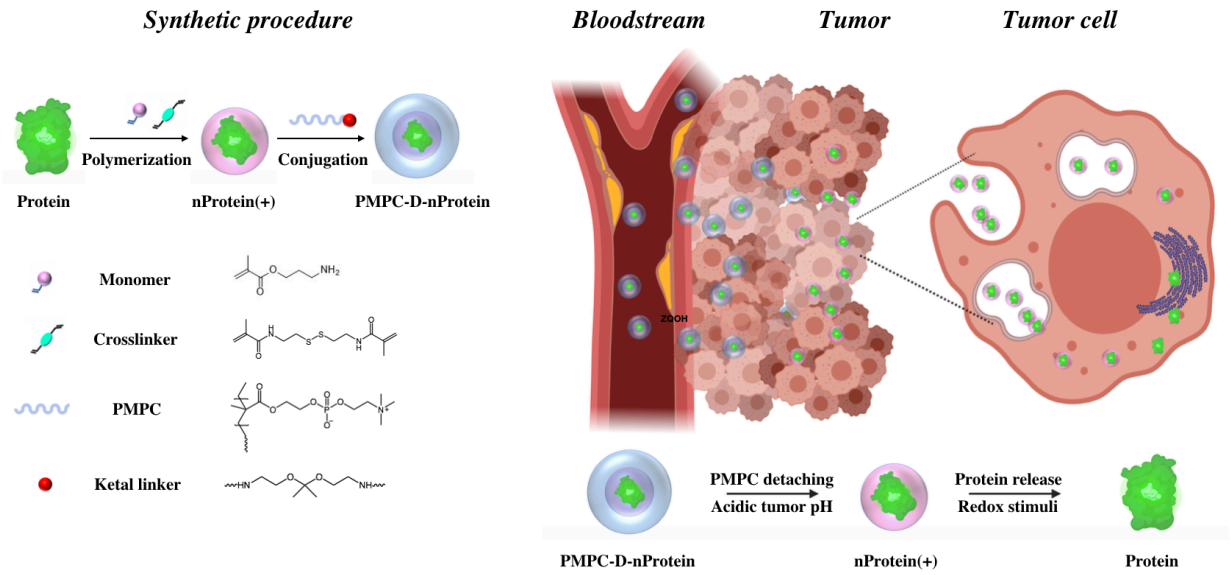

Figure 3-1 Illustration of sheddable PMPC conjugated nanocomplex that enables prolonged circulation, tumor accumulation, tissue penetration, cellular internalization, and tumor inhibition for the delivery of protein therapeutics to tumor.

3.2 Results and discussion

The construction process of nanocapsules and nanocomplexes is illustrated in Figure 3-1. We first synthesized positively charged BSA nanocapsules as described in the previous work[76]. The positively charged nanocapsule denoted as nBSA(+) was obtained by in situ polymerization with AAM and N-(3-Aminopropyl)methacrylamide (APM) as monomers, and N,N′-Bis(acryloyl)cystamine (CYSC) as the redox-degradable crosslinker (molar ratio of BSA, AAM, APM and CYSC is 1:4500:500:500), in which the monomer APM provided the positive charge. Then we modified the surface of nBSA(+) with Dibenzocyclooctyne (DBCO) and subsequently conjugated it with PMPC-ketal-Azide via click chemistry to obtain sheddable PMPC nanocomplex, which were denoted as PMPC-D-nBSA. While non-sheddable nanocomplex PMPC-ND-nBSA

was synthesize following a similar procedure with PMPC-Azide to serve as a control. Moreover, to investigate the stealth effect of zwitterionic polymer shell, we also synthesized non-zwitterionic BSA nanocapsule with a neutral surface charge as a negative control. The neutrally charged nanocapsule denoted as nBSA(o) was obtained following a similar procedure with the addition of negatively charged monomer acrylic acid (AA) to neutralize the positive charge from APM (molar ratio among BSA, AAM, APM, AA and CYSC is 1:4500:500:500:500). The successful construction of nanocapsules and nanocomplexes were confirmed by the size distribution and zeta potential test. As shown in the DLS result (Figure 3-2a), the diameter of nBSA(o) and nBSA(+) were both around 20 nm compared to 5 nm of native protein BSA, implying the formation of BSA encapsulated nanocapsules. While the nanocomplex PMPC-D-nBSA and PMPC-ND-nBSA both showed diameters that were around 10 nm larger than those of nanocapsules, suggesting the conjugation of PMPC chains onto the surface. The size distribution and spherical morphology of nanocapsule and nanocomplex were also observed in TEM figures (Figure 3-2e and f). As shown in Figure 3-2b, the zeta potential of native BSA was -5 mV while those of nBSA(+) and nBSA(o) were 6 mV and 0.5 mV, respectively, which demonstrated their positively and neutrally charged surface. After PMPC conjugation, both PMPC-ND-nBSA and PMPC-D-nBSA showed zeta potential of nearly 0 mV, suggesting the charge screening by the zwitterionic polymer. The surface charge was also confirmed by the agarose electrophoresis. As shown in Figure 3-2d, native BSA migrated toward positive direction while nBSA(+) moved to the negative direction, suggesting negative and positive surface charges, respectively. While nBSA(o), PMPC-ND-nBSA, and PMPC-D-nBSA all stayed in the well in electric field, showing neutral surface charges.

Once being intravenously administrated, nanoparticles are opsonized by serum proteins, which leads to the phagocytosis and immune clearance. Therefore, it is of prerequisite for the

nanoparticles to be capable of escaping the opsonization. To simulate the opsonization process, we incubated each sample with bovine serum at 37 ºC, followed by filtering and testing the amount of adsorbed serum protein using BCA assay. The same volume of PBS was also incubated with bovine serum as the control. As shown in Figure 3-2c, more than 25% of bovine serum protein adsorbed to nBSA(+) and nBSA(o) after 2 h incubation while less than 15% of bovine serum protein absorbed onto both PMPC-D-nBSA and PMPC-ND-nBSA, which was nearly consistent with that of PBS. This result implied that the anti-fouling PMPC shell was able to render nanoparticles resistance to protein adsorption whereas the neutral charge exclusively was not sufficient to provide such resistance.

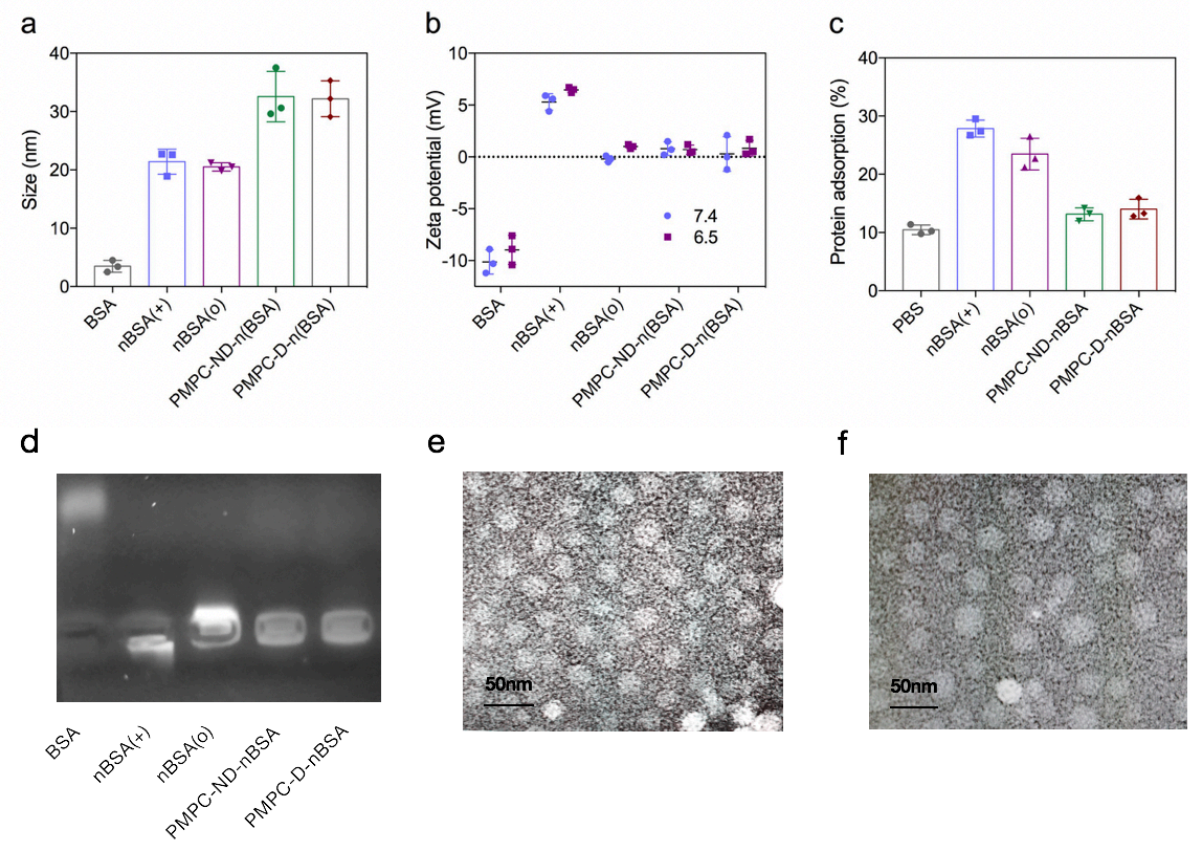

Figure 3-2 Structural characterization of nanocapsules and nanocomplexes. Size distribution (a), zeta potential (b), normalized protein adsorption (c), and agarose electrophoresis (d) of BSA, nBSA(o), nBSA(+), PMPC-ND-nBSA, and PMPC-D-nBSA. TEM images of nBSA(+) (e) and PMPC-D-nBSA (f)

With the resistance to opsonization, we then evaluated if the PMPC conjugated nanocapsule could escape from phagocytosis using macrophage cell line J774A.1 as the model. The nanocapsules and nanocomplexes were labeled with TAMRA dye and then incubated with J774A.1 cell for 2 h, respectively. As observed via fluorescent microscope (Figure 3-3), the fluorescent intensities in the cells incubated with PMPC-ND-nBSA and PMPC-D-nBSA were consistent, which were both much weaker than those in the cells incubated with nBSA(+) and nBSA(o). This suggests that the PMPC shell is able to prevent the internalization of nanocomplexes by macrophage. Based on the resistance of nanocomplexes to protein adsorption and phagocytosis in vitro, we reason that the PMPC conjugated nanocomplex is capable of escaping from opsonization and phagocytosis in vivo.

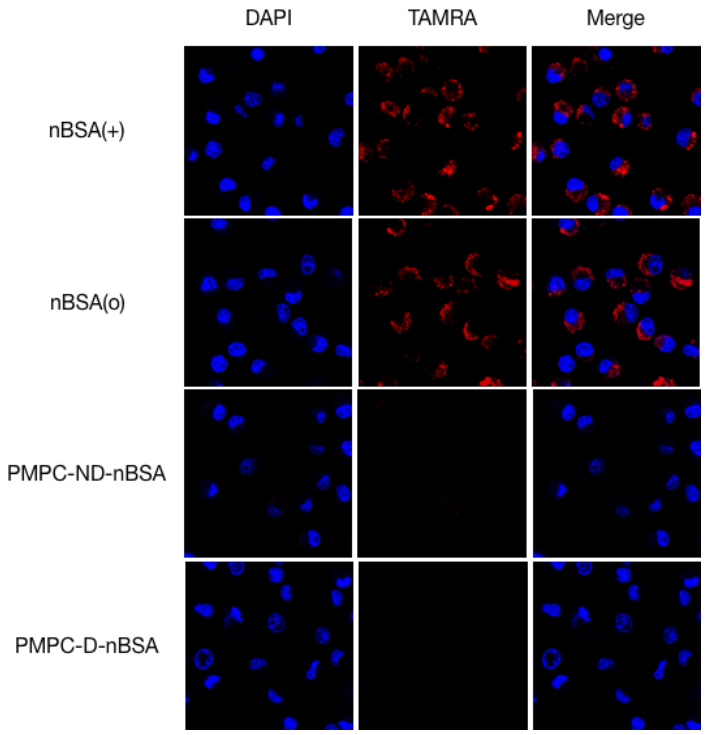

Figure 3-3 The cellular internalization of nanocapsules and nanocomplexes. CLSM images of J774A.1 cells incubated with nBSA(+), nBSA(o), PMPC-ND-nBSA, and PMPC-D-nBSA for 2 h. BSA was labeled with TAMRA fluorescent dye. The nucleus was labeled with DAPI.

The PMPC shell provides the nanocomplex with resistance to phagocytosis whereas such resistance also prevents their cellular uptake by tumor cells, leading to the failure of intracellular delivery. The pH-responsive ketal linker that connects the PMPC chain and nanocapsule has been demonstrated to be able to be broken down in response to the acidic tumor microenvironment, leading to the release of PMPC chains from the surface. To investigate the release rate of PMPC polymer, we dialyzed PMPC-ND-nBSA and PMPC-D-nBSA against buffers with pH value 7.4 and 6.5 at 37 ^{o}C, respectively. The amount of released PMPC polymer was determined by ^{1}H NMR

with an internal standard. As illustrated in Figure 3-3b, PMPC-D-nBSA released 18% of the conjugated PMPC polymer at pH value 7.4 while 75% at pH value 6.5, suggesting a remarkable increase in the release rate in the acidic environment. The detachment of PMPC chain recovers the positive surface charge of the nanocapsule, as demonstrated by the zeta potential test. The zeta potential of PMPC-D-nBSA increased from 0 mV to 4.7mV at pH value 6.5 while it only increased to 1.2 mV at pH value 7.4 (Figure 3-3c). Thus, we reason that the recovered positive charge can facilitate the cellular internalization of PMPC-D-nBSA in the tumor tissue. To verify it, we incubated TAMRA labeled PMPC-D-nBSA in pH 7.4 and 6.5 buffer at 37 ^{o}C for 48 h and then incubated them with 4T1 tumor cells, respectively. TAMRA labeled PMPC-D-nBSA was added directly to the cells without pre-incubation in the buffers served as the control. As observed in the fluorescent images (Figure 3-3a), the fluorescent intensity of PMPC-D-nBSA pre-incubated at pH value 7.4 for 48 h in 4T1 cell was almost identical to that without pre-incubation, which was much weaker than that pre-incubated at pH value 6.5 for 48 h. Such enhanced cellular internalization by tumor cells after the degradation of ketal linkers combined with the resistance to phagocytosis before the degradation suggests that PMPC-D-nBSA could prevent the immune clearance while penetrate into tumor cells in response to the acidic tumor environment.

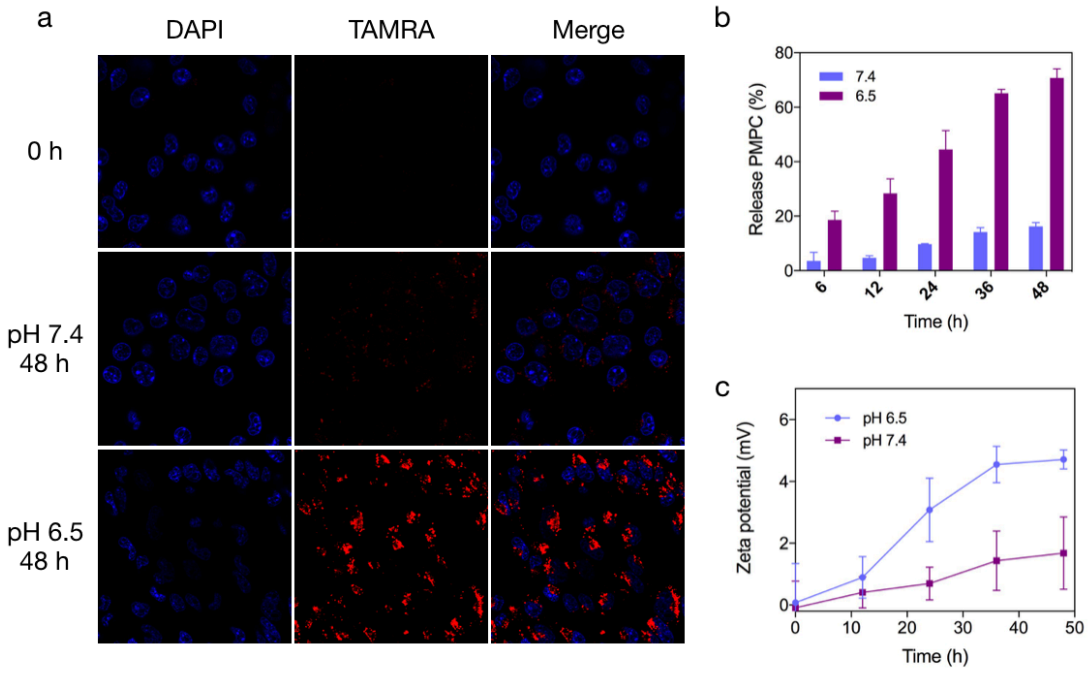

Figure 3-4 Enhanced cellular uptake of PMPC-D-nBSA in response to acidic stimuli. (a) CLSM images of 4T1 cells incubated with PMPC-D-nBSA, and PMPC-D-nBSA pre-incubated in PBS (pH 7.4) and PBS (pH 6.5) for 48 h. BSA was labeled with TAMRA fluorescent dye while the nucleus was labeled by DAPI. (b) The released PMPC polymer at different time points from the shell of PMPC-D-nBSA incubated in PBS (pH 7.4 and 6.5) at 37 ºC, respectively. (c) The change of zeta potential at different time points of PMPC-D-nBSA incubated in PBS (pH 7.4 and 6.5) at 37 ºC, respectively.

After being endocytosized by tumor cells, it is critical for the nanoparticle to escape from the endosomal organelles. Due to the protonation of amino groups on the surface in response to the acidic endosomal environment, the internalized PMPC-D-nBSA could disrupt the endosome and lysosome, leading to the leakage to cytosol. We incubated TAMRA labeled PMPC-D-nBSA that had pre-incubated in pH value 6.5 buffer at 37 ºC for 48 h with 4T1 tumor cells for 2 h or 12

h, followed by medium removal, washing, and staining the nucleus with Hoechst and the late endosome and lysosome with lysotracker deep red. The intracellular trafficking of the internalized PMPC-D-nBSA was then investigated by monitoring the colocalization between TAMRA and deep red fluorescent signals. After 2 h incubation, the overlap of PMPC-D-nBSA (red) with deep red (green) was at 90% colocalization, suggesting that the nanocomplex was endocytosized and trapped into endosomes. Whereas the degree of colocalization of decreased to 40% after 12 h incubation, indicating that the majority of the nanocomplexes had been escaped from the late endosome or lysosome and delivered into the cytosol (Figure 3-5).

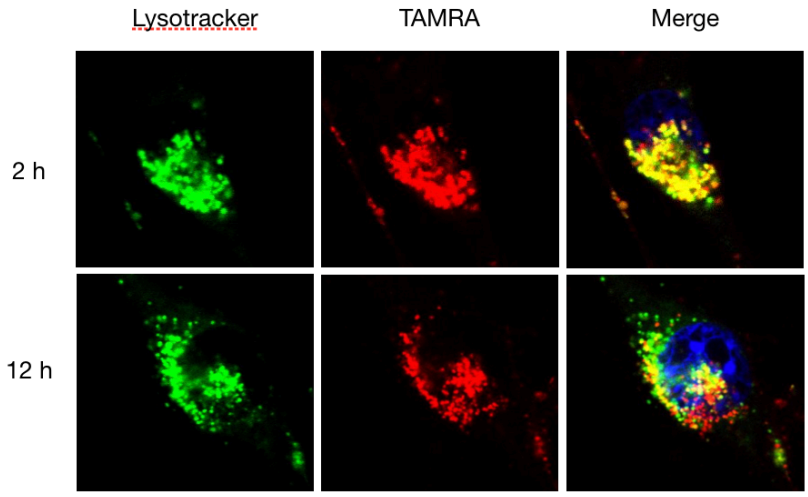

Figure 3-5 The intracellular trafficking of PMPC-D-nBSA. The CLSM images of 4T1 cells incubated with PMPC-D-nBSA for 2 h and 12 h, respectively. PMPC-D-nBSA was pre-incubated in PBS (pH 6.5) for 48 h prior to the addition to the cells. BSA was labeled with TAMRA while the lysosome and late endosome were labeled with lysotracker deep red.

Another obstacle that hampers the nanoparticle-based protein delivery is the tumor tissue penetration. It has been widely discussed by previous publications, yet no consensus conclusion has been reached. Some argued that the positive charge could facilitate tissue penetration through the electrostatic interactions between the nanoparticle and negatively charged tumor cell membrane. While others suggested that the neutral charge surface could reduce the adsorption of extracellular protein as well as the internalization by the periphery tumor cells, by which the tissue penetration could be enhanced. In this work, we assume that the anti-fouling surface could follow the second mechanism and enhance the tissue penetration due to its stronger resistance to the protein adsorption and cellular internalization compared to the non-zwitterionic counterparts. To demonstrated it, we simulated the tumor extracellular environment by culturing EGFP expressed MDA-MB-231 tumor cells with 50% extracellular matrix (ECM) in microchannels for 12 h. TAMRA labeled nBSA(+), nBSA(o), PMPC-ND-nBSA, and PMPC-D-nBSA were then added to each well on one side of the channel, respectively, followed by incubation at 37 ^{o}C for further 12 h. As observed in Figure 3-6a, the diffusion distances of nBSA(o) and nBSA(+) in the microchannel were almost consistent, which were much shorter than those of PMPC-ND-nBSA and PMPC-D-nBSA. Qualified by plotting the profile of distance vs fluorescence (Figure 3-6b), the relative fluorescent intensity of nBSA(o) and nBSA(+) decayed to less than 5% of the initial intensity at the distance of 4 mm while those of PMPC-D-nBSA and PMPC-ND-nBSA remained around 10% at the distance of 10 mm. Those results suggest an enhanced penetration in the tumor extracellular matrix that is facilitated by the zwitterionic shell. Furthermore, we investigated the 3D tumor penetration of the nanoparticles using a tumor spheroid model. As observed in CLSM (Figure 3-6c), the fluorescent signals of PMPC-ND-nBSA and PMPC-D-nBSA almost uniformly dispersed throughout the whole spheroid while those of nBSA(+) and nBSA(o) were trapped in

the peripherical area of the spheroid after 12 h incubation. Those results indicate an improved 3D tumor penetration of PMPC conjugated nanocomplexes over the non-conjugated nanocapsules.

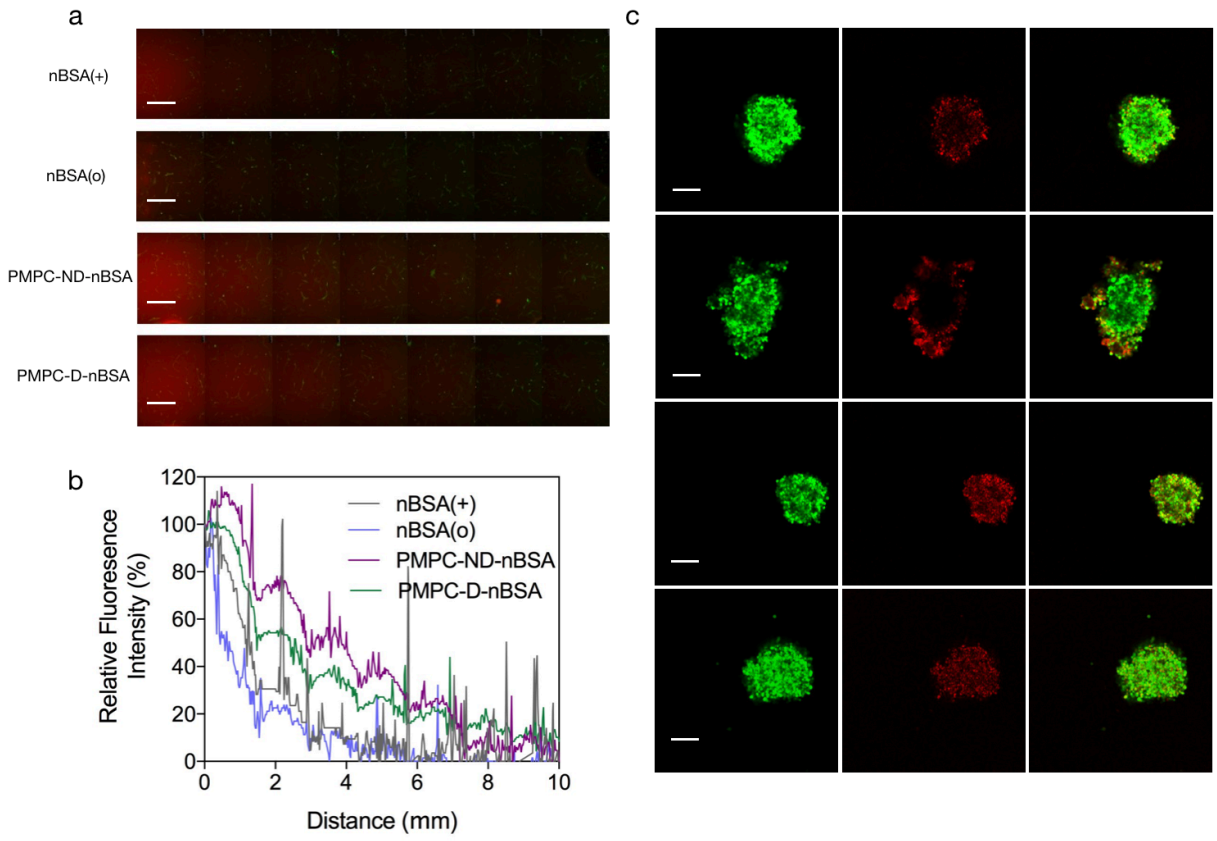

Figure 3-6 in vitro tissue penetration of nanocapsules and nanocomplexes. (a) Representative fluorescent images of TAMRA labeled nanocapsule diffusion distance in the channel with EGFP expressed MB-MDA-231 cells in 50% tumor extracellular matrix for 24 h. The scale bar represents 500 μm. (b) The normalized fluorescent intensity profile upon distance of nanocapsules in the channel. (c) CLSM images of the optical slices through the centers of 4T1 tumor spheroid co-incubated with nBSA(+), nBSA(o), PMPC-ND-nBSA, and PMPC-D-nBSA for 24 h. Scale bars = 100 μm.

Having confirmed the features of PMPC conjugated nanocomplexes in vitro, we then investigated their in vivo behavior. To study their circulation in the blood stream, we intravenously injected the TAMRA labeled nanocapsules and nanocomplexes to the mice (BALB/c). By testing the fluorescent intensity in the blood samples taken at each time point, the pharmacokinetic profiles were plotted. As illustrated in Figure 3-7a, the half-lives of PMPC-ND-nBSA and PMPC-D-nBSA were 30.6 h and 24.2 h, respectively, which were much longer than those of nBSA(o) and nBSA(+) (4.5 h and 3.6 h). That indicates a long-term circulation of nanocomplexes due to the anti-fouling PMPC shell, which provides a better opportunity for the nanocomplexes to leak from the blood vessel to the tumor site via the EPR effect. We next investigated the tumor accumulation of nanocapsules and nanocomplexes using live fluorescent imaging and organ imaging. The samples were labeled with Alexa fluor 647 dye and then intravenously injected to the mice (BALB/c). As shown in the live imaging and its quantified result (Figure 3-7b, d), PMPC-ND-nBSA and PMPC-D-nBSA both showed remarkable relative fluorescent intensity in tumors 6 h post-injection with mean fluorescent intensity of 11.9×10^9 and 9.8×10^9, which increased to 15.2×10^9 and 14.7×10^9 72 h post-injection, respectively. Whereas the nanocapsules showed negligible fluorescent intensity in tumors compared with those showed by nanocomplexes. Moreover, as shown in the organ fluorescent imaging and its quantified result 72 h post-injection (Figure 3-7 c, e), the nanocapsules showed much lower mean fluorescent intensities in the tumor than those in the liver and spleen while the nanocapsules showed consistent mean fluorescent intensities in the liver compared to those in the liver. Those results indicate that the PMPC conjugation could effectively reduce the clearance of nanocomplexes in the liver while boost their accumulation in the tumor.

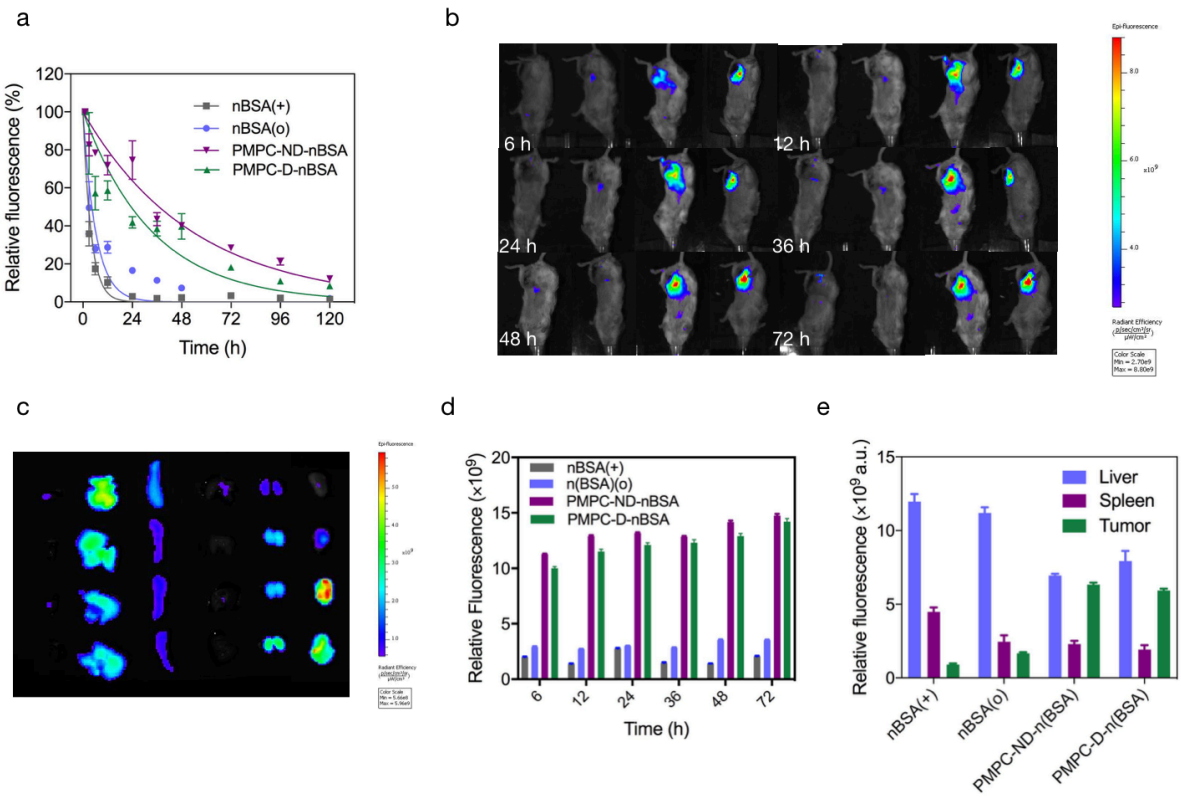

Figure 3-7 In vivo trafficking of nanocapsules and nanocomplexes. (a) Pharmacokinetics profile of nBSA(+), nBSA(o), PMPC-ND-nBSA, and PMPC-D-nBSA. The nanocapsules were labeled with TAMRA before being intravenously injected to mice (BALB/c). (b) Live imaging of nanocapsules in mice (BALB/c) at different time points after the intravenous injection. From left to right are nBSA(+), nBSA(o), PMPC-ND-nBSA, and PMPC-D-nBSA. (c) Organ fluorescent imaging of heart, liver, spleen, lung, and kidney 72 h after intravenous injection of nBSA(+), nBSA(o), PMPC-ND-nBSA, and PMPC-D-nBSA. (d) Relative fluorescence intensity of samples in the tumor of mice injected by nBSA(+), nBSA(o), PMPC-ND-nBSA, and PMPC-D-nBSA upon different times.(e) Relative fluorescence intensity of samples in liver, tumor. spleen of mice injected by nBSA(+), nBSA(o), PMPC-ND-nBSA, and PMPC-D-nBSA 72 h after the injection.

Given the ability to overcome those delivery barriers of PMPC conjugated nanocomplex, we next employed SAP as a ribosomal inactivating toxin to investigate its ability to deliver intracellularly functional protein for tumor inhibition. First, we synthesized sheddable PMPC conjugated SAP nanocomplex PMPC-D-nSAP and assessed the release of SAP in response to intracellular stimuli. Due to the disruption of disulfide bonds by glutathione (GSH), the nanocomplex released 75% of encapsulated SAP after incubation with 10 mM GSH for 72 h while that in PBS released less than 10%, reasoning an effective SAP release to the cytoplasm (Figure 3-8a). Then we evaluated the in vitro cytotoxicity of SAP nanocapsules and nanocomplexes in 4T1 tumor cells. As shown in Figure 3-8b, PMPC-D-nSAP that was pre-incubated in pH 6.5 buffer for 48 h displayed a tumor cell inhibition of 74%, which was slightly lower than that displayed by nSAP. Whereas native SAP and PMPC-D-nSAP that was pre-incubated in pH 7.4 buffer showed less than 20% of tumor cell inhibition, implying that PMPC-D-nSAP could exert tumor growth suppression upon the retention in the tumor tissue.

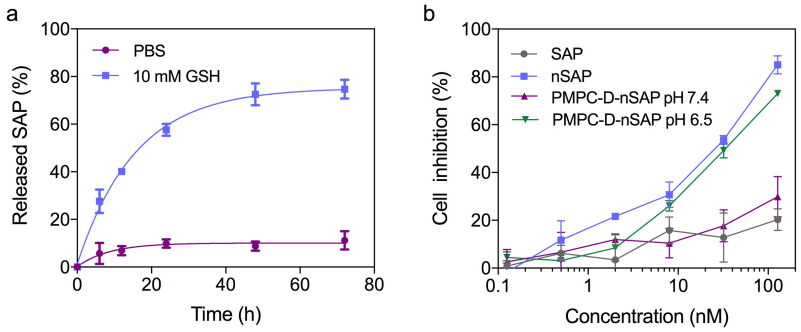

Figure 3-8 Tumor cell inhibition by nanocapsules and nanocomplexes. (a) Cumulative release of SAP from the PMPC-D-nSAP in 10 mM GSH at 37 ºC. PBS was used as the control. (b) The growth inhibition of 4T1 cells incubated with different concentrations of native SAP, nSAP, PMPC-D-nSAP pre-incubated in pH values 7.4 and 6.5 for 48 h, respectively.

Accordingly, we next investigated its in vivo therapeutic outcome by intravenously injecting native SAP, PMPC-ND-nSAP, and PMPC-D-nSAP to the 4T1 tumor bearing mice. PBS was injected as the negative control. As presented in Figure 3-8a, PBS, native SAP, and PMPC-ND-nBSA groups exhibited rapid increases in average tumor volume, which reached approximately 975 ± 59, 827 ± 27, and 839 ± 36 mm^3 at the endpoint on day 15, respectively. In the contrast, PMPC-D-nSAP exhibited a remarkable suppression tumor growth with the average tumor volume up to 369 ± 18 mm^3 at the end of the treatment period compared with other groups. As illustrated in Figure 3-8b, the body weight of mice in each group showed little change after 15-day period treatment, suggesting no severe side effect upon the administration of SAP samples. In addition, survival time was recorded after the treatment by SAP samples. As shown in Figs. 3-9 c and d, the mice in the groups treated with PMPC-D-nSAP revealed a significantly improved survival half-life (27 days) than those of the PBS, native SAP and PMC-D-nBSA groups (16, 17, and 17 days, respectively). Those results suggest that PMPC-D-nSAP is able to effectively suppress the tumor growth in vivo with negligible side effects.

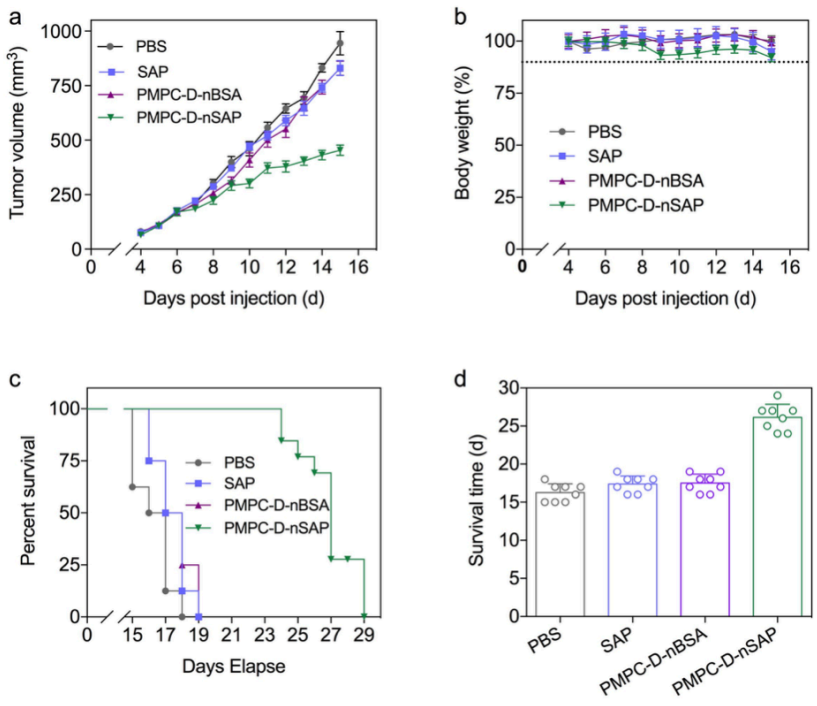

Figure 3-9 In vivo tumor suppression by PMPC-D-nSAP. (a) tumor volume, (b) body weight, (c) survival rate and (d) Body weight of 4T1 tumor-bearing mice administered with PBS, native SAP, PMPC-D-nBSA, and PMPC-D-nSAP by intravenous injection. The dosage of SAP was set to 0.6 mg/kg.

3.3 Conclusion and Prospects

We developed a novel protein delivery platform based on sheddable PMPC conjugated nanocomplex. With the Aid of PMPC shell, the nanocomplex is capable to escape from the immune clearance, prolong its circulation time, improve the tumor accumulation and penetration. In response to the acidic tumor microenvironment, the sheddable PMPC shell can be detached from the nanocomplex, which recovers its positive surface charge and enhances the internalization by tumor cells. Once being internalized by tumor cells, the amino group enables the endosomal

escape while the degradation of crosslinker enables the release of the protein. With ribosomal inactivating protein SAP as a model protein, we demonstrated that this novel type of nanocomplex has a great potential as a systemic protein delivery for tumor therapy.

In the future, based on the enhanced tumor penetration by PMPC shell, we plan to investigate the tissue penetration of nanoparticles with PMPC shell in healthy mice, which could be potentially used to solve the problem of anti-virus drug penetration in tissues. Moreover, we plan to conjugate certain ligands to the surface of nanocomplex to investigate if the active targeting could further enhance delivery efficacy.

3.4 Experimental section

3.4.1 Materials

SAP, BSA, AAM, MPC, Hexamine, 2,2-Bis(aminoethoxy)propane, Ethylenediamine, and 4-Cyano-4-(phenylcarbonothioylthio)pentanoic acid were purchased from Sigma Aldrich Inc. N,N‘-Bis(acryloyl)cystamine (CYSC), Tetramethylethylenediamine (TEMED), and 1-ethyl-3-(-3-dimethylaminopropyl) carbodiimide hydrochloride (EDC), N-hydroxysuccinimide(NHS), and 4,4′-Azobis(4-cyanovaleric acid were purchased from Thermofisher Inc. APM was purchased from Monomerpolymer Inc. Azide-NHS and DBCO-NHS was purchased from Click Chemistry Tools. TAMRA-NHS, FITC-NHS, and Alexa fluor 647-NHS, DAPI were purchased from Fluoroprobes Inc. Buffers are prepared following the methods depicted in the previous work. J774A.1 and 4T1 cells were purchased from American Type Culture Collection (ATCC). The

Dulbecco's Modified Eagle Medium (DMEM) growth medium, trypsin and Fetal Bovine Serum (FBS) was obtained from Corning.

3.4.2 Instruments

Uv adsorption, fluorescent intensity and spectra were recorded with a Tecan Infinite 200 PRO plate reader. ^{1}H NMR spectra were recorded with a Bruker AV400 broad band FT NMR spectrometer. Dynamic light scattering (DLS) studies of the enzyme nanocomplexes was measured on Zetasizer Nano instrument (Malvern Instruments Ltd., Kingdom). Transmission electron microscope (TEM) images were obtained on T12 Quick CryoEM and CryoET (FEI). The fluorescence microscope images were acquired by Leica dmi8 inverted microscope. The Confocal microscope images were obtained by Confocal SP8-STED/FLIM/FCS. The optical imaging and quantification were achieved by IVIS Lumina II (Perkin Elmer).

3.4.3 Synthesis of PMPC-ketal-Azide and PMPC-Azide

The typical protocols of PMPC polymers synthesis using RAFT polymerization are given as below. Briefly, monomer MPC (2.95 g, 10 mmol) was mixed with 4-Cyano-4-(phenylcarbonothioylthio)pentanoic acid (27.9 mg, 0.1 mmol) and initiator 4,4′-Azobis(4-cyanovaleric acid) (14 mg, 0.05 mmol) and dissolved into 10 mL anhydrous methanol. The mixture was degassed by nitrogen for 30 min, followed by polymerization at 65 ^{o}C for 6 h. After the reaction, the reaction mixture was poured into excess THF and washed for twice, followed by drying in vacuum to obtain PMPC polymer. The degree of polymerization was determined to be 90 measured by ^{1}H NMR.

Then we selected a two-step reaction with hexamine and MPC in one-pot to remove the phenyl groups of the chain transfer group on the terminal. Briefly, 2 g as-prepared PMPC90 (0.075 mM) was dissolved into 10 mL methanol, followed by the addition of 75 mg hexamine (0.75 mM), 45 mg MPC monomer (0.15 mM), and 2 mg 4,4′-Azobis(4-cyanovaleric acid) (0.0075 mM). The mixture was purged with nitrogen for 30 min, followed by incubation at 65 ^{o}C for 1 h. End-group removed PMPC90 was obtained by precipitation and wash by excess THF and subsequently dried in vacuum.

To convert the end-group of PMPC from carboxyl group to azide group, we designed a two-step process. First, the carboxyl groups are coupled with diamine to be transferred to the primary amine groups (PMPC-NH_2). As for the synthesis of PMPC-Azide, 1.6 g PMPC polymer (0.06 mM) was dissolved in 10 mL DI water, followed by addition of 120 mg EDC (0.6 mM) and 28 mg NHS (0.24 mM) in 500 uL pH 5.0 MES buffer. The mixture was stirred at 4 ^{o}C for 1 h to activate the carboxyl end-groups, after which 36 mg Ethylenediamine (0.6 mM) was added in. The reaction was allowed to last for 24 h. Then the mixture was dialyzed against DI water for 24 h to obtain the PMPC-NH_2 solution. Next, the amine group was coupled with azide-NHS to be eventually converted to maleimide group (PMPC-azide). Briefly, 10 mL PB buffer (pH 8.0) contained 1.6 g PMPC-NH_2 was added with 20 mg azide-NHS (0.06 mM). The coupling reaction was allowed to last for 2 h at room temperature. Then the unreacted azide-NHS was removed by Sephadex G25 column to obtain the final product. The synthesis of PMPC-ketal-azide followed a similar procedure as described above with changing diamine to 2,2-Bis(aminoethoxy)propane.

3.4.4 Synthesis of nanocapsule nBSA(+) and nBSA(o), and nSAP

The synthesis of nanocapsule nBSA(+) and nBSA(o) followed the procedure described in the previous work. For the synthesis of nBSA(+), 1 mg/mL BSA solution was added by 10% w/v APM, AAM, TEMED dissolved in water, and 5% w/v CYSC in DMSO. The mixture was vortexed for 10 s, followed by the addition of 10% APS to initiate the in situ polymerization. The feed molar ratio of BSA, APM, AAM, CYSC, TEMED, and APS were set to 1: 500: 4500: 500: 500: 500. The polymerization process was allowed to last for 2 h at 4 ^{o}C. Then the mixture was purified by DEAE column and subsequent dialysis against DI water for 24 h. The synthesis procedure of nBSA(o) was similar to that of nBSA(o). The feed molar ratio of BSA, APM, AA, AAM, CYSC, TEMED, and APS were set to 1: 500: 500: 4500: 500: 500: 500. As for the synthesis of nSAP, the BSA was changed to SAP with the feed ratio of SAP, APM, AAM, CYSC, TEMED, and APS setting to 1: 1000: 9500: 1000: 500: 500. The size, zeta potential and morphology of as-obtained nanocapsules were tested by DLS measurement, zeta-sizer and TEM, respectively. Then they were stored in the fridge for further test.

3.4.5 Synthesis of nanocomplex PMPC-D-nBSA, PMPC-ND-nBSA, and PMPC-D-nSAP

The Synthesis of nanocomplexes were conducted by conjugating PMPC polymer to the nanocapsules via click chemistry. Briefly, 1 mg/mL nanocapsule solution was mixed with 50 mg/mL PMPC polymer solution. The feed weight ratio of polymer to nanocapsule was set to 20: 1. HEPES buffer (500 mM, pH 7.4) was added in to adjust the pH to 7.4. The reaction was allowed to last for 24 h at 4 ^{o}C, followed by dialysis against DI water for 48 h at 4 ^{o}C to remove the unconjugated PMPC polymer (molecular weight cut-off, 100 kDa). The size, zeta potential and

morphology of as-obtained nanocomplexes were tested by DLS measurement, zeta-sizer and TEM, respectively. Then they were stored in the fridge for further test.

3.4.6 Agarose gel electrophoresis

First, native BSA, nBSA(+), nBSA(o), PMPC-ND-nBSA, and PMPC-D-nBSA were conjugated by TAMRA fluorescent dye. 1 mg/mL samples were added by 1% w/v TAMRA-NHS in DMSO with the feed molar ratio of 1:10. The pH value of the mixture was adjusted to 8.0 using HEPES buffer (500 mM pH 8.0). The reaction was allowed to incubate at 4 ^{o}C for 12 h, followed by purification using sephadex G-25 column to remove the unconjugated fluorescent dye. Then the TAMRA labeled samples was added to the agarose gel to run the electrophoresis at 120 mV for 12 min. The result was recorded by photography upon UV light (Ex: 365 nm).

3.4.7 Protein adsorption

The relative protein adsorption of each sample was determined following the method below: 40 μL nBSA(+), nBSA(o), PMPC-ND-nBSA, and PMPC-D-nBSA (1 mg/mL) were mixed with 20 μL of bovine serum and incubated at 37°C for 30 min, respectively. 40 μL PBS was used as the control. After incubation, samples were filtered and washed with 60 μL PBS for 3 times with centrifugal filtration (molecular weight cut-off, 100 kDa) to remove the unabsorbed serum proteins. After reconstituting with 60 μL of PBS, the amount of protein adsorbed was determined by measuring the overall protein concentration of each sample with BCA assay using mice serum as the standard.

3.4.8 Cellular internalization by macrophage

We selected J774.1A cell as the model immune cell line using the fluorescent microscope to evaluate the cellular uptake of TAMRA labeled nBSA(+), nBSA(o), PMPC-ND-nBSA, and PMPC-D-nBSA by the macrophage. Briefly, J774.1A cells were seeded into a 96-well plate (5×10^3 cells/well) and cultured in DMEM (normal level of glucose in medium, with 10% FBS and 100 μg/mL streptomycin and 100 U/mL penicillin) at 37 °C with 98% humidity and 5% CO_2 for 24 h prior to exposure to the samples. After the addition of 10 μL each sample (0.1 mg/mL corresponding to protein concentration) to the culturing medium respectively, cells were further incubated for 2 h at 37 °C. Then the cells were washed by cold PBS for 3 times to remove the samples. Cellular uptake of each sample was observed by the fluorescent microscope.

3.4.9 Detachment of PMPC polymer and surface charge recovery

The detachment of PMPC polymer from the nanocomplexes was determined by monitoring the release of PMPC chain at different pH values. Briefly, 500 μL PMPC-ND-nBSA and PMPC-D-nBSA were dialysis against 10 mL pH 7.4 and 6.5 PBS buffer at 37 °C, respectively (molecular weight cut-off, 100 kDa). 1 mL of release medium was withdrawn at each time point (0 h, 6 h, 12h, 24 h, 36 h, and 48 h), followed by lyophilization. The freeze-dried polymer was re-dissolved to deuterium and applied to ^{1}H NMR with an internal standard to determine the amount of PMPC polymer released.

To evaluate the recovery of surface charge, 500 μL PMPC-ND-nBSA and PMPC-D-nBSA were incubated in pH 6.5 and 7.4 HEPES buffer (25 mM) at 37 °C, respectively. At each pre-

determined time point (6 h, 12h, 24 h, 36 h, and 48 h), the samples were taken and applied to zeta potential measurement to determine their surface charges.

3.4.10 Cellular internalization by tumor cells

We selected 4T1 cell as the model tumor cell line using the fluorescent microscope to evaluate the cellular uptake of TAMRA labeled PMPC-D-nBSA by the tumor cells. Briefly, 4T1 cells were seeded into a 96-well plate (5×10^3 cells/well) and cultured in DMEM (normal level of glucose in medium, with 10% FBS and 100 μg/mL streptomycin and 100 U/mL penicillin) at 37 ^{o}C with 98% humidity and 5% CO_2 for 24 h prior to exposure to the samples. The samples were as-obtained PMPC-D-nBSA, PMPC-D-nBSA pre-incubated at pH 7.4 for 48 h, and PMPC-D-nBSA pre-incubated at pH 6.5 for 48 h. After the addition of 10 μL each sample (0.1 mg/mL corresponding to protein concentration) to the culturing medium, respectively, cells were further incubated for 2 h at 37 ^{o}C. Then the cells were washed by cold PBS for 3 times to remove the samples. Cellular uptake of each sample was observed by the fluorescent microscope.

3.4.11 Intracellular trafficking of PMPC-D-nBSA

4T1 cells were seeded on the CLSM cover glass and cultured in DMEM (normal level of glucose in medium, with 10% FBS and 100 μg/mL streptomycin and 100 U/mL penicillin) at 37 ^{o}C with 98% humidity and 5% CO_2 for 24 h prior to exposure to the samples (5×10^3 cell/well). TAMRA labeled PMPC-D-nBSA was pre-incubated in pH 6.5 PBS buffer at 37 ^{o}C for 48 h, followed by being added to the 4T1 cells at the final concentration of 0.05 mg/mL and incubated for 2 h and 12 h, respectively. The medium was replaced by fresh medium after the incubation.

The nucleus, late endosome and lysosome were stained by Hoechst and lysotracker deepred, respectively. Then the endosomal escape of PMPC-D-nBSA was observed by CLSM.

3.4.12 Nanoparticle diffusion in microchannels

EGFP expressed MDA-MB-231 cells were cultured in DMEM (normal level of glucose in medium, with 10% FBS and 100 μg/mL streptomycin and 100 U/mL penicillin) at 37 ^{o}C with 98% humidity and 5% CO_2 for 24 h. Then the cells were trypsinized, collected and mixed with tumor extracellular matrix at the volume ratio of 1:1 on ice (2.5×10^4/mL). 50 μL cell suspension was injected to each channel, followed by incubation at 37 ^{o}C with 98% humidity and 5% CO_2 for 4 h. 35 μL nBSA(+), nBSA(o), PMPC-ND-nBSA, PMPC-D-nBSA (0.1 mg/mL) were then added to the well on one side of each channel. The microchannel was allowed to incubate at 37 ^{o}C for 12 h, followed by being observed using fluorescent microscope to determine the nanoparticle diffusion in the channels. The histogram profiles of fluorescent signal in TAMRA channel (red) were then plotted using FIJI software.

3.4.13 Nanoparticle penetration in 3D tumor spheroid

3D tumor spheroid was cultured following the procedure below: 96 well-plate was added by 20 μl 1.5% agarose in DMEM in each well, followed by incubation at roome temperature for 2 h with an adhesive cover to obtain the agarose coated well-plate. EGFP expressed MDA-MB-231 cells were then cultured in DMEM (normal level of glucose in medium, with 10% FBS and 100 μg/mL streptomycin and 100 U/mL penicillin) at 37 ^{o}C with 98% humidity and 5% CO_2 for 24 h. The cells were trypsinized, collected and resuspended in the DMEM. Then 150 μL of the cell

suspension was added to each agarose coated well (5×10^3 cells/well). The well-plate was allowed to be incubated at 37 ºC for 4 days to obtain the tumor spheroid. Then TAMRA labeled nBSA(+), nBSA(o), PMPC-ND-nBSA and PMPC-D-nBSA were added to each well at the final concentration of 0.1 mg/mL and incubated at 37 ºC for 12 h. After the incubation, the spheroids were pipetted out and washed with cold PBS for 3 times, followed by being pipetted onto the CLSM cover glass and sealed. The sample penetration in 3D tumor spheroid was observed using CLSM. The histogram profiles of fluorescent signal in TAMRA channel (red) were then plotted using FIJI software.

3.4.14 Pharmacokinetics

Pharmacokinetics profiles of nanoparticles were accessed by monitoring the fluorescent intensity of TAMRA in plasma after intravenous administration. Briefly, 12 mice (BALB/C) were divided into 4 groups and intravenously injected with 150 μL TAMRA labeled nBSA(+), nBSA(o), PMPC-ND-nBSA, and PMPC-D-nBSA via the tail vein, respectively. The injection dosage of samples was set to 2.5 mg/kg. As a negative control, another 3 mice were injected with 150 μL of PBS. The blood samples (20 μL) were then taken from the tails at 1 h, 2 h, 4 h, 8 h, 12 h, 24 h, 36 h, 48 h, 72 h, 96 h, and 120 h post injection. The blood samples were centrifuged at 1000 rpm for 5 min to remove the blood cells, and the fluorescent intensity of TAMRA in the plasma was measured using plate reader (n=3). The analysis of the PK data was achieved by fitting the data using a one-phase exponential decay model with the constraints of $Y0 < 0.1$ (maximum BSA concentration cannot be higher than 0.1 mg/mL) and Plateau = 0.005354 (the mean background value from the negative control).

3.4.15 Biodistributions

The nanoparticle samples were labeled with Alexa fluor 647 before the administration. Briefly, 0.5 mL 1 mg/mL nBSA(+), nBSA(o), PMPC-ND-nBSA, and PMPC-D-nBSA were mixed with 20 μL HEPES 8.0 buffer and 1 μL 1% Alexa fluor 647 NHS ester in DMSO and allowed to incubate at 4 ºC for 12 h in dark, respectively. Then the mixtures were purified by sephadex G-25 column and stored at 4 ºC

For in vivo biodistribution studies, tumor xenografted mice were achieved by subcutaneously injecting 5×10^6 4T1 cells suspended in 100 μL of PBS/ECM (3/1, v/v) into the mice (BALB/c). The mice were fed for 14 days for the tumor growth.

Then 4 tumor bearing mice were intravenously injected with fluorescence labeled samples via the tail vein, respectively. The injection amount of each samples was set to 2.5 mg/kg. PBS was injected to the mouse as a control. At different time points (6 h, 12 h, 24 h, 36 h, 48 h, 72 h), the mice were applied to small animal live imaging to observe the tumor accumulation. The relative fluorescent intensity of each sample in the tumor was determined by ROI tools compared with that in the tumor injected by PBS (n=3). The mice were then perfused with PBS, followed by organs collection 72 h post injection. The fluorescent images of heart, liver, spleen, lung, and kidney were recorded by the organ fluorescent imaging. The relative fluorescent intensity of each organ was determined by ROI tools compared with that in the tumor injected by PBS (n=3)

3.4.16 SAP release test

SAP was labeled with TAMRA dye prior to the synthesis of PMPC-D-SAP. Cumulative SAP release from PMPC-D-nSAP was obtained by testing the fluorescent intensity of TAMRA labeled SAP. Briefly, 0.1 mL TAMRA labeled PMPC-D-nSAP (1 mg/mL) was added to dialysis tubing (Molecular weight cutoff: 100 kD) and dialyzed against 20 mL PBS or PBS with 10 mM GSH at 37 ºC. At each time point (0, 6, 12, 24, 48, 72 h), 1 mL of the release medium was taken while 1 mL fresh medium was supplied in. The fluorescent intensity of each aliquot was then recorded by plate reader (Ex: 550 nm, Em: 585 nm). The release experiment was repeated following the same procedure for another 2 times. Then the cumulative release profiles were plotted by the fluorescent intensity of release SAP at each time point normalized to the initial intensity (n=3).

3.4.17 Tumor cell growth inhibition test

Tumor cell growth inhibition by the SAP encapsulated nanoparticles was tested in 4T1 cell line. 4T1 cells were seeded to 96 well-plate in DMEM (normal level of glucose in medium, with 10% FBS and 100 μg/mL streptomycin and 100 U/mL penicillin) at 37 ºC with 98% humidity and 5% CO_2 for 24 h (1×10^4 per well). Native SAP, nSAP, PMPC-ND-nSAP, and PMPC-D-SAP were pre-incubated in pH 6.5 buffer at 37 ºC for 48 h and then added to each well, respectively. The final concentration gradient of each sample was set to 0.1, 0.5, 2, 8, 32, and 128 nM/mL (n=6). The cells were allowed to incubate with each sample for 72 h. Then resazurin (20 μL) was added into each well at the final concentration of 0.1 mg/mL and further incubated for 2 h. Quantification

of the cell viability was achieved by measuring the fluorescence intensities with a plate reader (Ex = 545 nm, Em = 585 nm).

3.4.18 In vivo anti-tumor activity

12 tumor bearing mice were divide into 4 groups (tumor volume approximately 50 mm^3). The mice were intravenously injected by PBS, native SAP, PMPC-D-nBSA, and PMPC-D-nSAP, respectively. The dosage of SAP was set to 0.6 mg/kg. The tumor volume. and body weight were recorded at different time points post-injection (4, 5, 6, 7, 8, 9, 10 ,11, 12, 13, 14, 15 h). Long-term survival was assessed with daily follow-up and individual sacrifice upon evidence of morbid disease progression.

Chapter 4 Conclusion

Protein therapeutics are considered to be advantageous over other types of therapeutics due to their high specificity, high efficiency and low side effect. However, the therapeutic applications of proteins are limited due to their fragile, immunogenic, and cell-impermeable natures and biological barriers in the delivery process. Although various strategies based on nanotechnology have been reported to alter the protein nature and overcome the biological barriers, those strategies usually focus on one or two biological barriers, thus leading to the undesirable protein delivery efficiency. Accordingly, it is still urgent to develop novel platforms to meet the requirements of protein delivery.

Our group has reported different strategies based on protein nanocapsule to overcome the biological barriers for the delivery of proteins. By rationally combining those strategies, I developed coacervate nanoreactors and sheddable PMPC conjugated nanocomplex for the delivery of proteins that target different sites.

As for the enzyme delivery to the blood stream, I developed the UOX/Cat enzyme cascade co-encapsulated coacervate nanoreactor with zwitterionic shell to enable a high structural and enzymatic stability, prolonged blood circulation time, effective reduction of uric acid level, and low side effect. As demonstrated, the enzyme cascade co-encapsulated nanoreactors can serve as a versatile platform for enzyme replacement therapy.

As for the systemic delivery of protein to the tumor cells, I developed sheddable PMPC conjugated nanocomplex to enable a prolonged circulation, tumor accumulation and penetration,

cellular internalization, endosomal escape and tumor inhibition. As proved, the novel type of nanocomplex can serve as platform to delivery functional proteins to the tumor cell for tumor therapy.

As summary, my research establishes novel designs to construct nanocarriers for protein delivery to achieve efficient delivery across various biological barriers.

References

1. J. C. Venter; M. D. Adams; E. W. Myers; P. W. Li; R. J. Mural; G. G. Sutton; H. O. Smith; M. Yandell; C. A. Evans; R. A. Holt, *Science* **2001,** *291* (5507), 1304-1351.

2. G. L. G. Miklos; R. Maleszka, *PROTEOMICS: International Edition* **2001,** *1* (2), 169-178.

3. D. S. Goodsell; A. J. Olson, *Annu. Rev. Biophys. Biomol. Struct.* **2000,** *29* (1), 105-153.

4. B. Leader; Q. J. Baca; D. E. Golan, *Nature reviews Drug discovery* **2008,** *7* (1), 21-39.

5. T. N. Seyfried; L. M. Shelton, *Nutr. Metab. (Lond.)* **2010,** *7* (1), 7.

6. D. Daneman, *The Lancet* **2006,** *367* (9513), 847-858.

7. E. J. Parkinson-Lawrence; T. Shandala; M. Prodoehl; R. Plew; G. N. Borlace; D. A. Brooks, *Physiology* **2010,** *25* (2), 102-115.

8. E. R. F. Collaboration, *N. Engl. J. Med.* **2011,** *364* (9), 829-841.

9. C. R. Kahn, *Diabetes* **1994,** *43* (8), 1066-1085.

10. T. Fukuda; L. Ewan; M. Bauer; R. J. Mattaliano; K. Zaal; E. Ralston; P. H. Plotz; N. Raben, *Annals of Neurology: Official Journal of the American Neurological Association and the Child Neurology Society* **2006,** *59* (4), 700-708.

11. R. Glew; A. Basu; E. Prence; A. Remaley, *Lab. Invest.* **1985,** *53* (3), 250-269.

12. M. Yu; J. Wu; J. Shi; O. C. Farokhzad, *J. Control. Release* **2016,** *240*, 24-37.

13. E. D. Kakkis; J. Muenzer; G. E. Tiller; L. Waber; J. Belmont; M. Passage; B. Izykowski; J. Phillips; R. Doroshow; I. Walot, *N. Engl. J. Med.* **2001,** *344* (3), 182-188.

14. R. Schiffmann; J. B. Kopp; H. A. Austin III; S. Sabnis; D. F. Moore; T. Weibel; J. E. Balow; R. O. Brady, *JAMA* **2001,** *285* (21), 2743-2749.

15. M. P. Whyte; C. R. Greenberg; N. J. Salman; M. B. Bober; W. H. McAlister; D. Wenkert; B. J. Van Sickle; J. H. Simmons; T. S. Edgar; M. L. Bauer, *N. Engl. J. Med.* **2012,** *366* (10), 904-913.

16. E. Beutler; A. Kay; A. Saven; P. Garver; D. Thurston; A. Dawson; B. Rosenbloom, **1991**.

17. S. H. Polmar; R. C. Stern; A. L. Schwartz; E. M. Wetzler; P. A. Chase; R. Hirschhorn, *N. Engl. J. Med.* **1976,** *295* (24), 1337-1343.

18. V. Valla, *Exp. Diabetes Res.* **2010,** *2010*.

19. L. G. Presta, *Curr. Opin. Biotechnol.* **1992,** *3* (4), 394-398.

20. P. J. Carter, *Nature reviews immunology* **2006,** *6* (5), 343-357.

21. G. P. Adams; L. M. Weiner, *Nat. Biotechnol.* **2005,** *23* (9), 1147-1157.

22. R. J. Benschop; C.-K. Chow; Y. Tian; J. Nelson; B. Barmettler; S. Atwell; D. Clawson; Q. Chai; B. Jones; J. Fitchett In *Development of tibulizumab, a tetravalent bispecific antibody targeting BAFF and IL-17A for the treatment of autoimmune disease*, MAbs, Taylor & Francis: 2019; pp 1175-1190.

23. A. C. Chan; P. J. Carter, *Nature Reviews Immunology* **2010,** *10* (5), 301-316.

24. A. Casadevall; E. Dadachova; L.-a. Pirofski, *Nature Reviews Microbiology* **2004,** *2* (9), 695-703.

25. D. M. Ecker; S. D. Jones; H. L. Levine In *The therapeutic monoclonal antibody market*, MAbs, Taylor & Francis: 2015; pp 9-14.

26. X. Wei; J. M. Decker; S. Wang; H. Hui; J. C. Kappes; X. Wu; J. F. Salazar-Gonzalez; M. G. Salazar; J. M. Kilby; M. S. Saag, *Nature* **2003,** *422* (6929), 307-312.

27. H. Hammers; E. R. Plimack; J. R. Infante; M. Ernstoff; B. I. Rini; D. F. McDermott; A. Razak; S. K. Pal; M. Voss; P. Sharma, *Ann. Oncol.* **2014,** *25* (suppl_4), iv361-iv362.

28. J. C. Bendell; T. W. Kim; B. C. Goh; J. Wallin; D.-Y. Oh; S.-W. Han; C. B. Lee; M. D. Hellmann; J. Desai; J. H. Lewin, Clinical activity and safety of cobimetinib (cobi) and atezolizumab in colorectal cancer (CRC). American Society of Clinical Oncology: 2016.

29. P. Simerska; T. Suksamran; Z. M. Ziora; F. de Labastida Rivera; C. Engwerda; I. Toth, *Vaccine* **2014,** *32* (37), 4743-4750.

30. J. Crosnier; P. Jungers; A. Couroucé; A. Laplanche; E. Benhamou; F. Degos; B. Lacour; P. Prunet; Y. Cerisier; P. Guesry, *The Lancet* **1981,** *317* (8224), 797-800.

31. W. Szmuness; C. E. Stevens; E. J. Harley; E. A. Zang; W. R. Oleszko; D. C. William; R. Sadovsky; J. M. Morrison; A. Kellner, *N. Engl. J. Med.* **1980,** *303* (15), 833-841.

32. I. Z. MacKenzie; J. Bichler; G. C. Mason; C. B. Lunan; P. Stewart; F. Al-Azzawi; M. De Bono; N. Watson; I. Andresen, *European Journal of Obstetrics & Gynecology and Reproductive Biology* **2004,** *117* (2), 154-161.

33. P. J. Nelson; A. J. Rees; M. D. Griffin; J. Hughes; C. Kurts; J. Duffield, *J. Am. Soc. Nephrol.* **2012,** *23* (2), 194-203.

34. N. Chirmule; V. Jawa; B. Meibohm, *The AAPS journal* **2012,** *14* (2), 296-302.

35. G. Gregoriadis; S. Jain; I. Papaioannou; P. Laing, *Int. J. Pharm.* **2005,** *300* (1-2), 125-130.

36. D. S. D'Astolfo; R. J. Pagliero; A. Pras; W. R. Karthaus; H. Clevers; V. Prasad; R. J. Lebbink; H. Rehmann; N. Geijsen, *Cell* **2015,** *161* (3), 674-690.

37. A. Lasser, *Hum. Pathol.* **1983,** *14* (2), 108-126.

38. D. A. Hume; I. L. Ross; S. R. Himes; R. T. Sasmono; C. A. Wells; T. Ravasi, *J. Leukoc. Biol.* **2002,** *72* (4), 621-627.

39. M. M. Frank; L. F. Fries, *Immunol. Today* **1991,** *12* (9), 322-326.

40. J. V. Sarma; P. A. Ward, *Cell Tissue Res.* **2011,** *343* (1), 227-235.

41. L. D. Leserman; J. N. Weinstein; R. Blumenthal; W. D. Terry, *Proceedings of the National Academy of Sciences* **1980,** *77* (7), 4089-4093.

42. A. Aderem; D. M. Underhill, *Annu. Rev. Immunol.* **1999,** *17* (1), 593-623.

43. R. S. Flannagan; V. Jaumouillé; S. Grinstein, *Annual Review of Pathology: Mechanisms of Disease* **2012,** *7*, 61-98.

44. M. Edidin, *Nature Reviews Molecular Cell Biology* **2003,** *4* (5), 414-418.

45. P. V. Del; A. Siflinger-Birnboim; J. Shepard; R. Bizios; J. Cooper; A. Malik In *Endothelial monolayer permeability to macromolecules*, Fed. Proc., 1987; pp 2511-2515.

46. J. Gruenberg; F. R. Maxfield, *Curr. Opin. Cell Biol.* **1995,** *7* (4), 552-563.

47. J. Huotari; A. Helenius, *The EMBO journal* **2011,** *30* (17), 3481-3500.

48. N. Oh; J.-H. Park, *International journal of nanomedicine* **2014,** *9* (Suppl 1), 51.

49. B. K. Shoichet; W. A. Baase; R. Kuroki; B. W. Matthews, *Proceedings of the National Academy of Sciences* **1995,** *92* (2), 452-456.

50. A.-S. Yang; B. Honig, *J. Mol. Biol.* **1993,** *231* (2), 459-474.

51. K. E. Tang; K. A. Dill, *J. Biomol. Struct. Dyn.* **1998,** *16* (2), 397-411.

52. R. L. Baldwin, *Biophys. J.* **1996,** *71* (4), 2056-2063.

53. C. Park; S. Marqusee, *Current protocols in protein science* **2006,** *46* (1), 20.11. 1-20.11. 14.

54. Y. Sonoda; S. Newstead; N.-J. Hu; Y. Alguel; E. Nji; K. Beis; S. Yashiro; C. Lee; J. Leung; A. D. Cameron, *Structure* **2011,** *19* (1), 17-25.

55. J. Jaspe; S. J. Hagen, *Biophys. J.* **2006,** *91* (9), 3415-3424.

56. R. Harada; N. Tochio; T. Kigawa; Y. Sugita; M. Feig, *JACS* **2013,** *135* (9), 3696-3701.

57. A. Ciechanover, *Nature reviews Molecular cell biology* **2005,** *6* (1), 79-87.

58. S. Frokjaer; D. E. Otzen, *Nature reviews drug discovery* **2005,** *4* (4), 298-306.

59. Z. Gu; A. Biswas; M. Zhao; Y. Tang, *Chem. Soc. Rev.* **2011,** *40* (7), 3638-3655.

60. S. Honary; F. Zahir, *Tropical Journal of Pharmaceutical Research* **2013,** *12* (2), 255-264.

61. M. L. Tan; P. F. Choong; C. R. Dass, *Peptides* **2010,** *31* (1), 184-193.

62. H. Liu; Y. Chen; Z. Shen; H. Frey, *React. Funct. Polym.* **2007,** *67* (2), 156-164.

63. A. Gallardo; F. Fernández; P. Bermejo; M. Rebuelta; A. Cifuentes; J.-C. Díez-Masa; J. San Román, *Biomaterials* **2000,** *21* (9), 915-921.

64. J. M. Harris; R. B. Chess, *Nature reviews Drug discovery* **2003,** *2* (3), 214-221.

65. Z. Amoozgar; Y. Yeo, *Wiley Interdisciplinary Reviews: Nanomedicine and Nanobiotechnology* **2012,** *4* (2), 219-233.

66. P. Zhang; F. Sun; S. Liu; S. Jiang, *J. Control. Release* **2016,** *244*, 184-193.

67. Q. Jin; Y. Chen; Y. Wang; J. Ji, *Colloids Surf. B. Biointerfaces* **2014,** *124*, 80-86.

68. C. Leng; X. Han; Q. Shao; Y. Zhu; Y. Li; S. Jiang; Z. Chen, *The Journal of Physical Chemistry C* **2014,** *118* (29), 15840-15845.

69. Y. Lee; T. Ishii; H. Cabral; H. J. Kim; J. H. Seo; N. Nishiyama; H. Oshima; K. Osada; K. Kataoka, *Angew. Chem. Int. Ed.* **2009,** *48* (29), 5309-5312.

70. G. V. Deodhar; M. L. Adams; B. G. Trewyn, *Biotechnology journal* **2017,** *12* (1), 1600408.

71. T. Nochi; Y. Yuki; H. Takahashi; S.-i. Sawada; M. Mejima; T. Kohda; N. Harada; I. G. Kong; A. Sato; N. Kataoka, *Nature materials* **2010,** *9* (7), 572-578.

72. E. Fröhlich, *International journal of nanomedicine* **2012,** *7*, 5577.

73. L. M. Vermeulen; S. C. De Smedt; K. Remaut; K. Braeckmans, *Eur. J. Pharm. Biopharm.* **2018,** *129*, 184-190.

74. D. K. Eggers; J. S. Valentine, *Protein Sci.* **2001,** *10* (2), 250-261.

75. J. Huang; Q. Shu; L. Wang; H. Wu; A. Y. Wang; H. Mao, *Biomaterials* **2015,** *39*, 105-113.

76. M. Yan; J. Du; Z. Gu; M. Liang; Y. Hu; W. Zhang; S. Priceman; L. Wu; Z. H. Zhou; Z. Liu, *Nature nanotechnology* **2010,** *5* (1), 48.

77. W. Wei; J. Du; J. Li; M. Yan; Q. Zhu; X. Jin; X. Zhu; Z. Hu; Y. Tang; Y. Lu, *Adv. Mater.* **2013,** *25* (15), 2212-2218.

78. S. Schoffelen; J. C. M. van Hest, *Soft Matter* **2012,** *8* (6), 1736-1746.

79. S. Shoda; H. Uyama; J. Kadokawa; S. Kimura; S. Kobayashi, *Chem. Rev.* **2016,** *116* (4), 2307-2413.

80. T. Hudlicky; J. W. Reed, *Chem. Soc. Rev.* **2009,** *38* (11), 3117-3132.

81. S. Mann, *Angewandte Chemie-International Edition* **2008,** *47* (29), 5306-5320.

82. R. J. Conrado; J. D. Varner; M. P. DeLisa, *Curr. Opin. Biotechnol.* **2008,** *19* (5), 492-499.

83. R. J. Ellis, *Trends Biochem. Sci* **2001,** *26* (10), 597-604.

84. P. Baumann; M. Spulber; O. Fischer; A. Car; W. Meier, *Small* **2017,** *13* (17).

85. K. Maximova; J. Wojtczak; J. Trylska, *Anal. Biochem.* **2019,** *567*, 96-105.

86. E. W. Miles; S. Rhee; D. R. Davies, *J. Biol. Chem.* **1999,** *274* (18), 12193-12196.

87. Y.-H. P. Zhang, *Biotechnol. Adv.* **2011,** *29* (6), 715-725.

88. W. N. Kelley; F. M. Rosenbloom; J. F. Henderson; J. E. Seegmiller, *Proc. Natl. Acad. Sci. U. S. A.* **1967,** *57* (6), 1735.

89. G. A. Grabowski; R. J. Hopkin, *Annual review of genomics and human genetics* **2003,** *4* (1), 403-436.

90. R. O. Brady; R. Schiffmann, *The Lancet Neurology* **2004,** *3* (12), 752-756.

91. E. F. Neufeld, Enzyme replacement therapy–a brief history. In *Fabry disease: perspectives from 5 years of FOS*, Oxford PharmaGenesis: 2006.

92. R. J. Desnick, *J. Inherit. Metab. Dis.* **2004,** *27* (3), 385-410.

93. M. E. Glasner; J. A. Gerlt; P. C. Babbitt, *Adv. Enzymol. Relat. Areas Mol. Biol.* **2007,** *75*, 193-239, xii-xiii.

94. N. Dahiya; R. Tewari; G. S. Hoondal, *Appl. Microbiol. Biotechnol.* **2006,** *71* (6), 773-782.

95. S. Violante; M. Berisa; T. H. Thomas; J. R. Cross, Stable Isotope Tracers for Metabolic Pathway Analysis. In *High-Throughput Metabolomics*, Springer: 2019; pp 269-283.

96. H. P. Modarres; M. Mofrad; A. Sanati-Nezhad, *RSC advances* **2016,** *6* (116), 115252-115270.

97. X. Fang; J. Huang; R. Zhang; F. Wang; Q. Zhang; G. Li; J. Yan; H. Zhang; Y. Yan; L. Xu, *J. Chem. Inf. Model.* **2019,** *59* (11), 4833-4843.

98. Y. Zhang; P. Ertbjerg, *Food Chem.* **2019,** *299*, 125104.

99. P. Kolhe; S. Goswami, Bulk Protein Solution: Freeze–Thaw Process, Storage and Shipping Considerations. In *Challenges in Protein Product Development*, Springer: 2018; pp 313-336.

100. M. P. Jackson; E. W. Hewitt, *Essays Biochem.* **2016,** *60* (2), 173-180.

101. P. Bohley; P. O. Seglen, *Experientia* **1992,** *48* (2), 151-157.

102. H. Schellekens, *Clin. Ther.* **2002,** *24* (11), 1720-1740.

103. M. Kessler; D. Goldsmith; H. Schellekens, *Nephrology Dialysis Transplantation* **2006,** *21* (suppl_5), v9-v12.

104. M. Baker; H. M. Reynolds; B. Lumicisi; C. J. Bryson, *Self/nonself* **2010,** *1* (4), 314-322.

105. X. Liu; Z. Zhang; Y. Zhang; Y. Guan; Z. Liu; J. Ren; X. Qu, *Adv. Funct. Mater.* **2016,** *26* (43), 7921-7928.

106. F. G. Sheikh; K. Pahan; M. Khan; E. Barbosa; I. Singh, *Proceedings of the National Academy of Sciences* **1998,** *95* (6), 2961-2966.

107. S. A. Comhair; P. R. Bhathena; R. A. Dweik; M. Kavuru; S. C. Erzurum, *The Lancet* **2000,** *355* (9204), 624.

108. R. Chandrawati; F. Caruso, *Langmuir* **2012,** *28* (39), 13798-13807.

109. D. M. Vriezema; P. M. Garcia; N. Sancho Oltra; N. S. Hatzakis; S. M. Kuiper; R. J. Nolte; A. E. Rowan; J. C. van Hest, *Angew. Chem.* **2007,** *119* (39), 7522-7526.

110. L. Hosta-Rigau; M. J. York-Duran; Y. Zhang; K. N. Goldie; B. Städler, *ACS applied materials & interfaces* **2014,** *6* (15), 12771-12779.

111. E. Rideau; R. Dimova; P. Schwille; F. R. Wurm; K. Landfester, *Chem. Soc. Rev.* **2018,** *47* (23), 8572-8610.

112. J. Liang; F. Mazur; C. Tang; X. Ning; R. Chandrawati; K. Liang, *Chemical science* **2019,** *10* (34), 7852-7858.

113. W.-H. Chen; M. Vázquez-González; A. Zoabi; R. Abu-Reziq; I. Willner, *Nature Catalysis* **2018,** *1* (9), 689-695.

114. F. P. Chang; Y. P. Chen; C. Y. Mou, *Small* **2014,** *10* (22), 4785-4795.

115. D. Xu; H. Han; Y. He; H. Lee; D. Wu; F. Liu; X. Liu; Y. Liu; Y. Lu; C. Ji, *Adv. Mater.* **2018,** *30* (22), 1707443.

116. Y. Liu; J. Du; M. Yan; M. Y. Lau; J. Hu; H. Han; O. O. Yang; S. Liang; W. Wei; H. Wang, *Nature nanotechnology* **2013,** *8* (3), 187.

117. A. F. Mason; J. C. van Hest, *Emerging Topics in Life Sciences* **2019,** *3* (5), 567-571.

118. D. S. Williams; A. J. Patil; S. Mann, *Small* **2014,** *10* (9), 1830-1840.

119. X. Lian; Y. Fang; E. Joseph; Q. Wang; J. Li; S. Banerjee; C. Lollar; X. Wang; H.-C. Zhou, *Chem. Soc. Rev.* **2017,** *46* (11), 3386-3401.

120. M. Yoshimoto; Y. Miyazaki; M. Sato; K. Fukunaga; R. Kuboi; K. Nakao, *Bioconjug. Chem.* **2004,** *15* (5), 1055-1061.

121. D. Gräfe; J. Gaitzsch; D. Appelhans; B. Voit, *Nanoscale* **2014,** *6* (18), 10752-10761.

122. X.-y. Zhang; P.-y. Zhang, *Current Nanoscience* **2017,** *13* (2), 124-129.

123. P. J. Photos; L. Bacakova; B. Discher; F. S. Bates; D. E. Discher, *J. Control. Release* **2003,** *90* (3), 323-334.

124. E. Casals; V. F. Puntes, *Nanomedicine* **2012,** *7* (12), 1917-1930.

125. M. Yan; J. Du; Z. Gu; M. Liang; Y. Hu; W. Zhang; S. Priceman; L. Wu; Z. H. Zhou; Z. Liu, *Nature nanotechnology* **2010,** *5* (1), 48-53.

126. S. Liang; Y. Liu; X. Jin; G. Liu; J. Wen; L. Zhang; J. Li; X. Yuan; I. S. Chen; W. Chen, *Nano Research* **2016,** *9* (4), 1022-1031.

127. X. Zhang; D. Xu; X. Jin; G. Liu; S. Liang; H. Wang; W. Chen; X. Zhu; Y. Lu, *J. Control. Release* **2017,** *255*, 54-61.

128. M. Zhao; D. Xu; D. Wu; J. W. Whittaker; R. Terkeltaub; Y. Lu, *Nano Research* **2018,** *11* (5), 2682-2688.

129. M. Jaturanpinyo; A. Harada; X. Yuan; K. Kataoka, *Bioconjug. Chem.* **2004,** *15* (2), 344-348.

130. M. Ma; B. Ahsan; J. Wang; M. Wang; X. Guo; M. A. C. Stuart; J. Wang, *Soft Matter* **2019,** *15* (41), 8210-8218.

131. A. M. Klibanov, *Trends Biotechnol.* **1997,** *15* (3), 97-101.

132. V. Stepankova; S. Bidmanova; T. Koudelakova; Z. Prokop; R. Chaloupkova; J. Damborsky, *Acs Catalysis* **2013,** *3* (12), 2823-2836.

133. C.-C. Lin; S. M. Sawicki; A. T. Metters, *Biomacromolecules* **2008,** *9* (1), 75-83.

134. J. F. Le Meins; O. Sandre; S. Lecommandoux, *The European Physical Journal E* **2011,** *34* (2), 14.

135. I. Louzao; J. C. M. van Hest, *Biomacromolecules* **2013,** *14* (7), 2364-2372.

136. G. Ke; M. Liu; S. Jiang; X. Qi; Y. R. Yang; S. Wootten; F. Zhang; Z. Zhu; Y. Liu; C. J. Yang, *Angew. Chem.* **2016,** *128* (26), 7609-7612.

137. R. L. Wortmann, *Curr. Opin. Rheumatol.* **2002,** *14* (3), 281-286.

138. P. J. Cannon; W. B. Stason; F. E. Demartini; S. C. Sommers; J. H. Laragh, *N. Engl. J. Med.* **1966,** *275* (9), 457-464.

139. M. Murea, *Adv. Chronic Kidney Dis.* **2012,** *19* (6), 419-424.

140. M. R. Sherman; M. G. Saifer; F. Perez-Ruiz, *Adv. Drug Del. Rev.* **2008,** *60* (1), 59-68.

141. H. U. Bergmeyer; E. Bernt, UV-Assay with Pyruvate and NADH. In *Methods of Enzymatic Analysis (Second Edition)*, Bergmeyer, H. U., Ed. Academic Press: 1974; pp 574-579.

142. V. T. DeVita; E. Chu, *Cancer Res.* **2008,** *68* (21), 8643-8653.

143. G. Delaney; S. Jacob; C. Featherstone; M. Barton, *Cancer: Interdisciplinary International Journal of the American Cancer Society* **2005,** *104* (6), 1129-1137.

144. A. R. Asthagiri; N. Pouratian; J. Sherman; G. Ahmed; M. E. Shaffrey, *Neurol. Clin.* **2007,** *25* (4), 975-1003.

145. N. Shinoura; R. Yamada; Y. Tabei; K. Saito; Y. Suzuki; K. Yagi, *Br. J. Neurosurg.* **2011,** *25* (2), 218-224.

146. X. Sui; R. Chen; Z. Wang; Z. Huang; N. Kong; M. Zhang; W. Han; F. Lou; J. Yang; Q. Zhang, *Cell Death Dis.* **2013,** *4* (10), e838-e838.

147. C. Lerman; B. Rimer; B. Blumberg; S. Cristinzio; P. F. Engstrom; N. MacElwee; K. O'Connor; J. Seay, *Cancer Nurs.* **1990,** *13* (5), 308-315.

148. J. R. Kintzing; M. V. F. Interrante; J. R. Cochran, *Trends Pharmacol. Sci.* **2016,** *37* (12), 993-1008.

149. H. D. Lagassé; A. Alexaki; V. L. Simhadri; N. H. Katagiri; W. Jankowski; Z. E. Sauna; C. Kimchi-Sarfaty, *F1000Research* **2017,** *6*.

150. X. Qin; C. Yu; J. Wei; L. Li; C. Zhang; Q. Wu; J. Liu; S. Q. Yao; W. Huang, *Adv. Mater.* **2019,** *31* (46), 1902791.

151. G. L. Plosker; D. P. Figgitt, *Drugs* **2003,** *63* (8), 803-843.

152. D.-H. Kong; M. R. Kim; J. H. Jang; H.-J. Na; S. Lee, *Int. J. Mol. Sci.* **2017,** *18* (8), 1786.

153. T. Kazemi; V. Younesi; F. Jadidi-Niaragh; M. Yousefi, *Artificial cells, nanomedicine, and biotechnology* **2016,** *44* (3), 769-779.

154. P. Berraondo; M. F. Sanmamed; M. C. Ochoa; I. Etxeberria; M. A. Aznar; J. L. Pérez-Gracia; M. E. Rodríguez-Ruiz; M. Ponz-Sarvise; E. Castañón; I. Melero, *Br. J. Cancer* **2019,** *120* (1), 6-15.

155. A. H. Staudacher; M. P. Brown, *Br. J. Cancer* **2017,** *117* (12), 1736-1742.

156. T. Ji; J. Lang; B. Ning; F. Qi; H. Wang; Y. Zhang; R. Zhao; X. Yang; L. Zhang; W. Li, *Adv. Mater.* **2019,** *31* (6), 1804395.

157. A. Sun; L. Z. Benet, *Pharmacology* **2020,** *105* (3-4), 145-163.

158. E. Cruz; V. Kayser, *Biologics: targets & therapy* **2019,** *13*, 33.

159. H. Chen; J. Li; W. Tan, *Advances in Breast Cancer Research* **2017,** *6* (4), 93-99.

160. S. Bobisse; P. G. Foukas; G. Coukos; A. Harari, *Annals of translational medicine* **2016,** *4* (14).

161. L. Ren; J. Lv; H. Wang; Y. Cheng, *Angew. Chem.* **2020,** *132* (12), 4741-4749.

162. A. Macone; S. Masciarelli; F. Palombarini; D. Quaglio; A. Boffi; M. C. Trabuco; P. Baiocco; F. Fazi; A. Bonamore, *Sci. Rep.* **2019,** *9* (1), 1-7.

163. J. H. E. Baker; A. H. Kyle; S. A. Reinsberg; F. Moosvi; H. M. Patrick; J. Cran; K. Saatchi; U. Häfeli; A. I. Minchinton, *Clin. Exp. Metastasis* **2018,** *35* (7), 691-705.

164. G. M. Thurber; M. M. Schmidt; K. D. Wittrup, *Adv. Drug Del. Rev.* **2008,** *60* (12), 1421-1434.

165. Y. Zhang; J. J. Røise; K. Lee; J. Li; N. Murthy, *Curr. Opin. Biotechnol.* **2018,** *52*, 25-31.

166. P. Lönn; A. D. Kacsinta; X.-S. Cui; A. S. Hamil; M. Kaulich; K. Gogoi; S. F. Dowdy, *Sci. Rep.* **2016,** *6* (1), 1-9.

167. Z. Shen; A. Fisher; W. K. Liu; Y. Li, PEGylated "stealth" nanoparticles and liposomes. In *Engineering of Biomaterials for Drug Delivery Systems*, Elsevier: 2018; pp 1-26.

168. Y. Men; S. Peng; P. Yang; Q. Jiang; Y. Zhang; B. Shen; P. Dong; Z. Pang; W. Yang, *ACS applied materials & interfaces* **2018,** *10* (28), 23509-23521.

169. M. Ray; Y.-W. Lee; F. Scaletti; R. Yu; V. M. Rotello, *Nanomedicine* **2017,** *12* (8), 941-952.

170. A. Jhaveri; V. Torchilin, *Expert opinion on drug delivery* **2016,** *13* (1), 49-70.

171. S. A. Smith; L. I. Selby; A. P. Johnston; G. K. Such, *Bioconjug. Chem.* **2018,** *30* (2), 263-272.

172. Z. Zhang; H. Wang; T. Tan; J. Li; Z. Wang; Y. Li, *Adv. Funct. Mater.* **2018,** *28* (40), 1801840.

173. M. Zhao; B. Hu; Z. Gu; K.-I. Joo; P. Wang; Y. Tang, *Nano Today* **2013,** *8* (1), 11-20.

174. M. Zhao; A. Biswas; B. Hu; K.-I. Joo; P. Wang; Z. Gu; Y. Tang, *Biomaterials* **2011,** *32* (22), 5223-5230.

175. J. Wen; S. M. Anderson; J. Du; M. Yan; J. Wang; M. Shen; Y. Lu; T. Segura, *Adv. Mater.* **2011,** *23* (39), 4549-4553.